

# Origin of Life Molecules in the Atmosphere After Big Impacts on the Early Earth

NICHOLAS F. WOGAN,<sup>1,2</sup> DAVID C. CATLING,<sup>1,2</sup> KEVIN J. ZAHNLE,<sup>3,2</sup> AND ROXANA LUPU<sup>4</sup>

<sup>1</sup>*Department of Earth and Space Sciences, University of Washington, Seattle, WA 98195*

<sup>2</sup>*Virtual Planetary Laboratory, University of Washington, Seattle, WA 98195*

<sup>3</sup>*Space Science Division, NASA Ames Research Center, Moffett Field, CA 94035*

<sup>4</sup>*BAER Institute, NASA Ames Research Center, Moffett Field, CA 94035*

## ABSTRACT

The origin of life on Earth would benefit from a prebiotic atmosphere that produced nitriles, like HCN, which enable ribonucleotide synthesis. However, geochemical evidence suggests that Hadean air was relatively oxidizing with negligible photochemical production of prebiotic molecules. These paradoxes are resolved by iron-rich asteroid impacts that transiently reduced the entire atmosphere, allowing nitriles to form in subsequent photochemistry. Here, we investigate impact-generated reducing atmospheres using new time-dependent, coupled atmospheric chemistry and climate models, which account for gas-phase reactions and surface-catalysis. The resulting H<sub>2</sub>-, CH<sub>4</sub>- and NH<sub>3</sub>-rich atmospheres persist for millions of years, until hydrogen escapes to space. HCN and HCCCN production and rainout to the surface can reach 10<sup>9</sup> molecules cm<sup>-2</sup> s<sup>-1</sup> in hazy atmospheres with a mole ratio of CH<sub>4</sub>/CO<sub>2</sub> > 0.1. Smaller CH<sub>4</sub>/CO<sub>2</sub> ratios produce HCN rainout rates < 10<sup>5</sup> molecules cm<sup>-2</sup> s<sup>-1</sup>, and negligible HCCCN. The minimum impactor mass that creates atmospheric CH<sub>4</sub>/CO<sub>2</sub> > 0.1 is 4 × 10<sup>20</sup> to 5 × 10<sup>21</sup> kg (570 to 1330 km diameter), depending on how efficiently iron reacts with a steam atmosphere, the extent of atmospheric equilibration with an impact-induced melt pond, and the surface area of nickel that catalyzes CH<sub>4</sub> production. Alternatively, if steam permeates and deeply oxidizes crust, impactors ∼ 10<sup>20</sup> kg could be effective. Atmospheres with copious nitriles have > 360 K surface temperatures, perhaps posing a challenge for RNA longevity, although cloud albedo can produce cooler climates. Regardless, post-impact cyanide can be stockpiled and used in prebiotic schemes after hydrogen has escaped to space.

## 1. INTRODUCTION

Two essential aspects of life are a genome and catalytic reactions, so the presence of ribonucleotide molecular “fossils” in modern biochemistry (White 1976; Goldman & Kacar 2021) and the ability of RNAs to store genetic information and catalyze reactions have led to the hypothesis that RNA-based organisms originated early (Cech 2012). This hypothesis proposes a stage of primitive life with RNA as a self-replicating genetic molecule that evolved by natural selection, which, at some point, became encapsulated in a cellular membrane and may have interacted with peptides from the beginning in the modified hypothesis of the RNA-Peptide World (e.g. Di Giulio 1997; Muller et al. 2022). In any case, RNA must be produced abiotically on early Earth for such scenarios. Chemists have proposed several prebiotic schemes that require nitriles - hydrogen cyanide (HCN), cyanoacetylene (HCCCN), cyanamide (H<sub>2</sub>NCN), and cyanogen (NCCN) - to synthesize ribonucleobases, which are building blocks of RNA (Benner et al. 2020; Sutherland 2016; Yadav et al. 2020).

Abiotic synthesis of nitriles in nature is known to occur efficiently from photochemistry in reducing N<sub>2</sub>-CH<sub>4</sub> atmospheres (Zahnle 1986; Tian et al. 2011). Indeed, Titan’s atmosphere, composed of mostly N<sub>2</sub> and CH<sub>4</sub>, makes HCN, HCCCN and NCCN (Strobel et al. 2009).

Geochemical evidence does not favor a volcanic source for a CH<sub>4</sub>-rich prebiotic atmosphere. Redox proxies in old rocks indicate that Earth’s mantle was only somewhat more reducing 4 billion years ago (Aulbach & Stagno 2016; Nicklas 2019). Therefore, volcanoes would have mostly produced relatively oxidized gases like H<sub>2</sub>O, CO<sub>2</sub> and N<sub>2</sub> instead of highly reduced equivalents, H<sub>2</sub>, CH<sub>4</sub> and NH<sub>3</sub> (Holland 1984; Catling & Kasting 2017; Wogan et al. 2020). Thus, steady-state volcanism would have likely produced Hadean air with CO<sub>2</sub> and N<sub>2</sub> as bulk constituents, whereas reducing gases, such as CH<sub>4</sub>, would have been minor or very minor.

However, Urey (1952) suggested that the prebiotic atmosphere was transiently reduced by large asteroid impacts. In more detail, Zahnle et al. (2020) argued that iron-rich impact ejecta could react with an impact-vaporized ocean to generate  $\text{H}_2$  ( $\text{Fe} + \text{H}_2\text{O} \leftrightarrow \text{FeO} + \text{H}_2$ ). As the  $\text{H}_2\text{O}$ - and  $\text{H}_2$ -rich atmosphere cools, their chemical equilibrium modeling with parameterized quenching finds that  $\text{H}_2$  can combine with atmospheric  $\text{CO}$  or  $\text{CO}_2$  to generate  $\text{CH}_4$ . After several thousand years of cooling, the steam condenses to an ocean, leaving a  $\text{H}_2$  dominated atmosphere containing  $\text{CH}_4$ . Zahnle et al. (2020) used a photochemical box model to show that such a reducing atmosphere would have generated prebiotic molecules like  $\text{HCN}$ . The reducing atmospheric state terminates when  $\text{H}_2$  escapes to space after millions of years.

Model simplicity in Zahnle et al. (2020) left critical questions unanswered. Their model of a cooling steam post-impact atmosphere did not explicitly simulate chemical kinetics pertinent to Earth, which may inaccurately estimate the generated  $\text{CH}_4$ . Additionally, their photochemical box model did not include all relevant reactions or distinguish between different prebiotic nitriles (e.g.  $\text{HCN}$  and  $\text{HCCCN}$ ). Finally, Zahnle et al. (2020) only crudely computed the climate of post-impact atmospheres, yet surface temperature is important for understanding the possible fate of prebiotic feedstock molecules. These molecules are needed to initiate prebiotic synthesis and must be available in the prebiotic environment.

Here, we improve upon the calculations made in Zahnle et al. (2020) using more sophisticated and accurate models of post-impact atmospheres. We estimate post-impact  $\text{H}_2$  production by considering reactions between the atmosphere and delivered iron, and equilibration between the atmosphere and impact-generated melt. Our model explicitly simulates the 0-D chemical kinetics of a cooling steam atmosphere, considering gas-phase reactions, as well as reactions occurring on nickel surfaces which catalyze  $\text{CH}_4$  production given that nickel is expected to be delivered by big impactors. After post-impact steam condenses to an ocean, we simulate the long-term evolution of a reducing atmosphere with a 1-D photochemical-climate model, quantifying  $\text{HCN}$  and  $\text{HCCCN}$  production and the climate in which they are deposited on Earth’s surface. Additionally, we discuss the possible fate and preservation of prebiotic molecules in ponds or lakes on Hadean land. Finally, we discuss how “lucky” primitive life was if created by post-impact molecules, given a need to not be subsequently annihilated by further impactors.

## 2. METHODS

We organize our investigation of post-impact Hadean atmospheres in three phases of atmospheric evolution depicted in Figure 1. Below, we briefly describe our numerical models for each phase and complete descriptions can be found in the Appendix.

In Phase 1, an impactor collides with Earth, vaporizing the ocean, and  $\text{H}_2$  is generated by reactions between the atmosphere and iron-rich impact ejecta, and atmospheric reactions with an impact-produced melt pond. Our model of this phase (Appendix A) accounts for  $\text{H}_2$  generation from impactor iron by assuming each mole of iron delivered to the atmosphere removes one mole of oxygen. For example, Fe can sequester O atoms from steam:



Simulations that consider reactions between the atmosphere and impact-melted crust follow a similar procedure to the one described in Itcovitz et al. (2022). Our model requires that the atmosphere and melt have the same oxygen fugacity. The oxygen fugacity of the melt is governed by relative amounts of ferric and ferrous iron (Kress & Carmichael 1991):



We assume that oxygen atoms can flow from the atmosphere into the melt (or visa-versa), and use an equilibrium constant for Reaction 2 from Kress & Carmichael (1991). Finally, we compute a chemical equilibrium state of the atmosphere (or atmosphere-melt system) at 1900 K using thermodynamic data from NIST for 96 gas-phase species (Appendix C.2). The result gives the estimated amount of  $\text{H}_2$  generated by an impact.

In Phase 2 of Figure 1, the steam atmosphere cools for thousands of years generating  $\text{CH}_4$  and  $\text{NH}_3$ , and eventually, the steam condenses to an ocean. We simulate these events with the 0-D kinetics-climate box model fully described in Appendix B. The gas-phase model tracks 96 species connected by 605 reversible reactions (Appendix C.2), but we do not account for photolysis. The model also optionally accounts for reactions that occur on nickel surfaces using the chemical network described in Schmider et al. (2021). As discussed later in Section 3.2, nickel is potentially delivered to

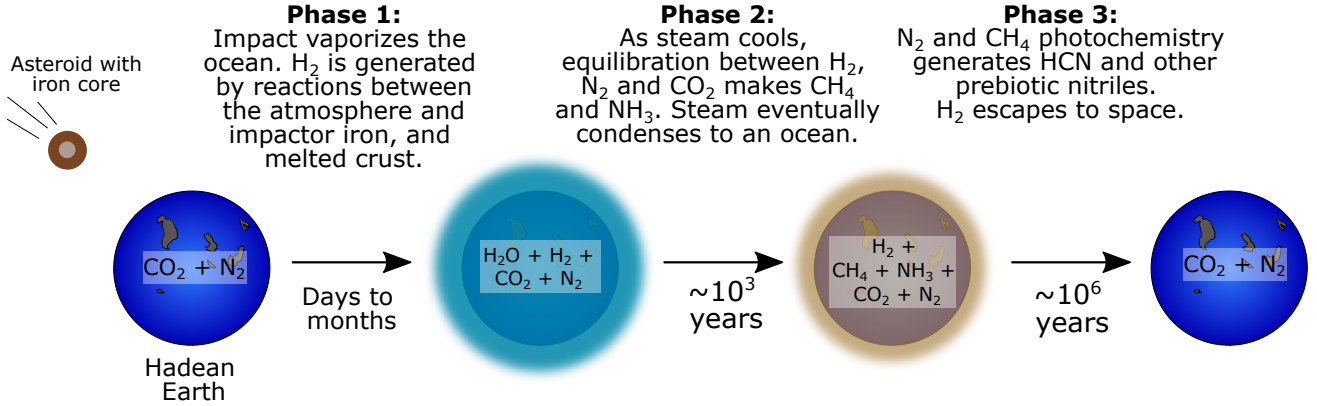


**Figure 1.** The three phases of atmospheric evolution after a large asteroid impact on the Hadean Earth. In Phase 1, the impactor vaporizes the ocean and heats up the atmosphere. Iron delivered by the impactor reacts with hot steam to make  $H_2$ .  $H_2$  is also modulated by equilibration between the atmosphere and an impact-generated melt pond. In Phase 2, as the steam-rich atmosphere cools for thousands of years,  $H_2$  reacts with  $CO_2$  to make atmospheric  $CH_4$ . Ultimately, the steam condenses to an ocean. Finally, in Phase 3,  $N_2$  and  $CH_4$  photochemistry generates HCN and other prebiotic nitriles. The  $H_2$  dominated atmosphere escapes to space over millions of years, causing the return of a more oxidizing  $N_2$  and  $CO_2$  atmosphere.

Earth’s surface by impacts which may catalyze methane production. In the model, atmospheric temperature changes as energy is radiated to space and is modulated by latent heat released from water condensation. We estimate the net energy radiated to space by using a parameterization of calculations performed with our radiative transfer code (Appendix D).

During Phase 3, photochemistry generates HCN and other prebiotic molecules. Hydrogen in the  $H_2$  dominated atmosphere escapes to space over millions of years, ushering in the return of a  $CO_2$  and  $N_2$  atmosphere. We use our time-dependent photochemical-climate model, *Photochem* (Appendix C), to simulate this phase of atmospheric evolution. The model solves a system of partial differential equations approximating molecular transport in the vertical direction and the effect of chemical reactions, photolysis, condensation, rainout in droplets of water, and atmospheric escape. Our reaction network (Appendix C.2) acceptably reproduces the steady-state composition of Earth and Titan (Appendix Figure A9). We evolve the model equations accurately over time using the CVODE Backward Differential Formula (BDF) method (Hindmarsh et al. 2005). As the atmosphere evolves, we compute self-consistent temperature structures using the radiative transfer code described and validated in Appendix D.

### 3. RESULTS

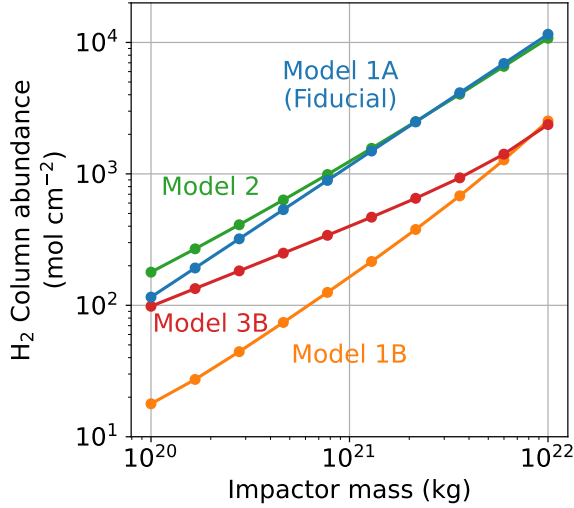
The following sections simulate the three post-impact phases of atmospheric evolution shown in Figure 1 for impactor masses between  $10^{20}$  and  $10^{22}$  kg (360 to 1680 km diameter) under various modeling assumptions.

#### 3.1. Phase 1: Reducing the steam-generated atmosphere with impactor iron

Within days, a massive asteroid impact would leave the Hadean Earth with a global  $\sim 2000$  K rock and iron vapor atmosphere, the iron derived from the impactor’s core (Itcovitz et al. 2022). In the following months to years, energy radiated downward from the silicates would vaporize a large fraction of the ocean, adding steam to the atmosphere (Sleep et al. 1989). At this point, steam should rapidly react with iron to generate  $H_2$ . Eventually, the iron vapor and then rock would rain out leaving behind a steam-dominated atmosphere containing  $H_2$ , as well as  $CO_2$  and  $N_2$  from the pre-impact atmosphere. The sequence of metal followed by silicate condensation with falling temperature is loosely analogous to that of the well-known condensation sequence of the solar nebula.

Furthermore, the massive impact would generate a melt pool on Earth’s surface inside the impact crater, which may contain reducing impact-derived iron. The atmosphere and melt pool could react to a redox-equilibrium state. This could add or sequester  $H_2$  from the atmosphere, depending on whether the melt was more or less reducing than the atmosphere (Itcovitz et al. 2022).

Recently, Itcovitz et al. (2022) used a smoothed-particle hydrodynamics (SPH) code with  $0.5 \times 10^6$  -  $3 \times 10^6$  particles of 150 - 250 km diameter to estimate the amount of  $H_2$  generated as these processes unfold under several different



Model 1A: 100% of impactor iron reacts with atmosphere. No melt-atmosphere reaction.

Model 1B: 15 - 30% of impactor iron reacts with atmosphere (Citron and Steward 2022). No melt-atmosphere reaction.

Model 2: 100% of impactor iron reacts with atmosphere. Includes melt-atmosphere reactions.

Model 3B: 15 - 30% of impactor iron reacts with atmosphere (Citron and Steward 2022). Includes melt-atmosphere reactions.

**Figure 2.** Post-impact  $H_2$  generation as a function of impactor mass under different modeling assumptions. Models 1A, 1B, 2 and 3B are identical to those describe in Figure 1 of Itcovitz et al. (2022). The simulation’s pre-impact volatile inventories, impact angle, and impact velocity are listed in Table 1. In Model 1A, all iron delivered by an impact reacts with steam to produce  $H_2$ . The resulting atmosphere does not equilibrate with a impact-generated melt pool. Model 1B assumes that a fraction ( $\sim 15\%$  to  $\sim 30\%$ ) of impactor iron reduces the steam atmosphere based on SPH simulations (Citron & Stewart 2022), and that the atmosphere is chemically isolated from a melt pool. Model 2 is like Model 1A while also including post-impact equilibration with a melt pool with a redox state of  $\Delta FMQ-2.3$  to represent peridotite (Itcovitz et al. 2022). Model 3B assumes that a fraction ( $\sim 15\%$  to  $\sim 30\%$ ) of impactor iron reacts with the steam atmosphere based on SPH simulations, and includes melt-atmosphere redox equilibration with a pool magma initially at  $\Delta FMQ-2.3$ . As stated in Section 3.1, we nominally assume Model 1A throughout the main text calculations. We also include simulations in the appendix that instead adopt Model 1B, which we consider to be a plausible lower bound for post-impact  $H_2$  generation.

impact scenarios on the Hadean Earth. In their fiducial case (i.e. their “Model 1A”), they assume that 100% of iron delivered by an impactor is available to react and reduce a post-impact steam atmosphere. In another scenario, they assume that only  $\sim 15 - 30\%$  of impactor iron reacts with the steam atmosphere based on their SPH simulations (their “Model 1B”) (Citron & Stewart 2022). For both cases, they also consider equilibration between the atmosphere and a melt pool (their “Model 2”, “Model 3A” and “Model 3B”). In their simulations, the melt pool is extremely reducing or more oxidizing depending on whether they assume it contains a fraction of the impactor’s iron, and they use SPH models to predict the amount of iron accreted to the melt pool (Citron & Stewart 2022). Overall, they conclude that melt-atmosphere equilibration generates about as much  $H_2$  as their fiducial case as long as the iron delivered to the melt-atmosphere system can equilibrate. However, if iron delivered to the melt pool sinks into Earth and cannot react with the atmosphere, then approximately 2 - 10 times less  $H_2$  is produced compared to their fiducial scenario (see the erratum in Itcovitz et al. (2022)).

Itcovitz et al. (2022) considers impactors between  $2 \times 10^{21}$  and  $2 \times 10^{22}$  kg, and assumes the pre-impact Earth has 1.85 oceans of water, 100 bars  $CO_2$  and 2 bars of  $N_2$ . However, we investigate impacts as small as  $10^{20}$  kg, and our nominal model (Table 1) assumes only 0.5 bars of pre-impact  $CO_2$  motivated by models of the Hadean carbonate-silicate cycle (Kadota et al. 2020) and assuming little mantle-hosted carbonate is vaporized. Therefore, we use a similar model (Appendix A) to the one described in Itcovitz et al. (2022) to predict the post-impact  $H_2$  for our alternative model assumptions (Table 1) and impactor sizes. Figure 2 shows the results.

Our calculations give two end-member scenarios for impact  $H_2$  production which we consider for subsequent calculations in this article. The more optimistic case assumes that 100% of the impactor’s iron reacts with an atmosphere that is chemically isolated from a melt pool (“Model 1A” in Figure 2). Following Zahnle et al. (2020), we adopt this scenario as our nominal model throughout the main text. This assumption produces a similar amount of  $H_2$  as an atmosphere-melt system that retains most of the impactor’s iron (e.g. “Model 2” in Figure 2), which is consistent with Itcovitz et al. (2022). The “Model 2” calculation assumes the melt pool has an initial oxygen fugacity of  $\Delta FMQ-2.3$

**Table 1.** Nominal model assumptions

Parameter	symbol	value
Pre-impact ocean inventory	$N_{\text{H}_2\text{O}}$	$1.5 \times 10^4 \text{ mol cm}^{-2}$ (i.e. 1 ocean)
Pre-impact $\text{CO}_2$ inventory	$N_{\text{CO}_2}$	$12.5 \text{ mol cm}^{-2}$ (i.e. “0.5 bars”)
Pre-impact $\text{N}_2$ inventory	$N_{\text{N}_2}$	$36 \text{ mol cm}^{-2}$ (i.e. “1 bar”)
Impactor mass	$M_{\text{imp}}$	$10^{20} - 10^{22} \text{ kg}$
Iron mass fraction of the impactor	$m_{\text{Fe,imp}}$	0.33
Fraction of iron that reacts with atmosphere	$X_{\text{Fe,atmos}}$	$1.0^a$
Impact angle	-	$45^\circ$
Impact velocity relative to Earth	-	$20.7 \text{ km s}^{-1}$
Eddy diffusion coefficient <sup>b</sup>	$K_{zz}$	$10^6 \text{ cm}^2 \text{ s}^{-1}$
Aerosol particle radius <sup>b</sup>	-	$0.1 \mu\text{m}$
Troposphere relative humidity	$\phi$	1
Surface Albedo	$A_s$	0.2
Temperature of the stratosphere	$T_{\text{strat}}$	200 K
Rainfall rate	$R_{\text{rain}}$	$1.1 \times 10^{17} \text{ molecules cm}^{-2} \text{ s}^{-1}$ (Modern Earth’s value)
HCN deposition velocity <sup>c</sup>	$v_{\text{dep,HCN}}$	$7 \times 10^{-3} \text{ cm s}^{-1}$
HCCCN deposition velocity <sup>d</sup>	$v_{\text{dep,HCCCN}}$	$7 \times 10^{-3} \text{ cm s}^{-1}$

<sup>a</sup> This is the “Model 1A” scenario for  $\text{H}_2$  production described near the end of Section 3.1 and in Figure 2.

<sup>b</sup> Assumed to be constant as a function of altitude.

<sup>c</sup> Estimated based on the HCN hydrolysis rate in the ocean (Appendix C.4).

<sup>d</sup> Assumed to be the same as HCN.

which is appropriate for a peridotite melt (Itcovitz et al. 2022).<sup>1</sup> However, our results are not sensitive to this assumption because, for “Model 2”, initial melt oxygen fugacities between  $\Delta\text{FMQ}$  and  $\Delta\text{FMQ}-4$  changes the generated  $\text{H}_2$  by a factor of at most  $\sim 1.3$ .

The less-optimistic case for  $\text{H}_2$  production is “Model 1B” in Figure 2, which assumes that only a fraction of the impactor iron reacts with an atmosphere, and that the latter does not react with a melt pool. We compute the fraction of available iron by extrapolating SPH simulations of impacts traveling at twice Earth’s escape velocity and colliding with Earth at a  $45^\circ$  angle (Appendix Figure A1), which is the most probable angle (Citron & Stewart 2022). Most simulations shown in the main text have a complementary figure in the Appendix that makes this alternative pessimistic assumption regarding post-impact  $\text{H}_2$  generation.

### 3.2. Phase 2: The cooling post-impact steam atmosphere

After reactions between impact-derived iron and steam produce  $\text{H}_2$ , the atmosphere would radiate at a rate determined by the optical properties of water vapor (Zahnle et al. 2020). Chemical reactions would initially be rapid, forcing the whole atmosphere to chemical equilibrium. Methane is thermodynamically preferred at lower temperatures, so it should become more abundant as the atmosphere cools. Eventually the atmosphere would reach a temperature where the reactions producing methane would be extremely sluggish compared to the rate of atmospheric cooling. At this point, the methane abundance would freeze, or quench. Ammonia would exhibit the same behavior as methane by initially rising in abundance then quenching when kinetics become slow. After several thousand years, water vapor condenses and rains out of the atmosphere to form an ocean.

We use the 0-D kinetics-climate box model described in Appendix B to simulate these events. By simulating each elementary chemical reaction, the model automatically computes methane and ammonia quenching as the atmosphere

<sup>1</sup> FMQ is the fayalite-magnetite-quartz redox buffer. See Chapter 7 in Catling & Kasting (2017) for a discussion of redox buffers.



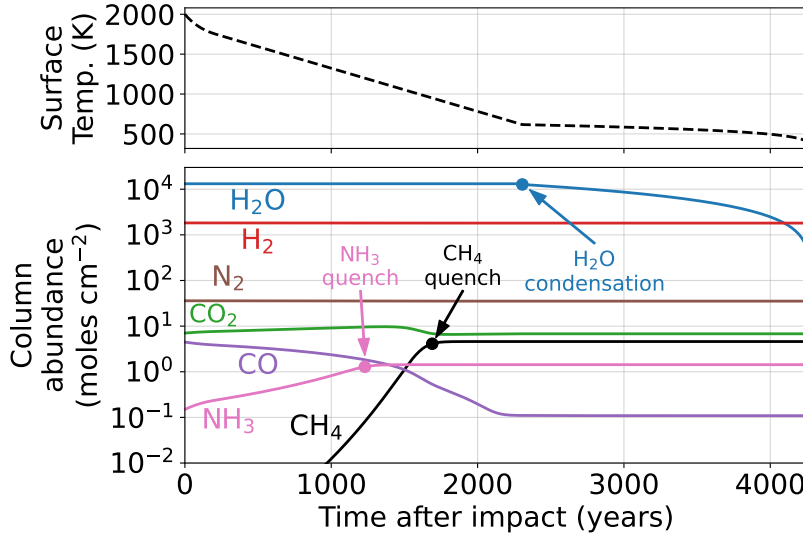


**Figure 3.** A kinetics-climate simulation of a cooling steam atmosphere caused by a  $1.58 \times 10^{21}$  kg impactor. The model uses the Table 1 nominal parameters. The top panel is surface temperature and the bottom panel shows atmospheric composition.

cools and temperature-dependent reactions slow. We first consider gas-phase kinetics, and later we will also consider nickel-surface kinetics.

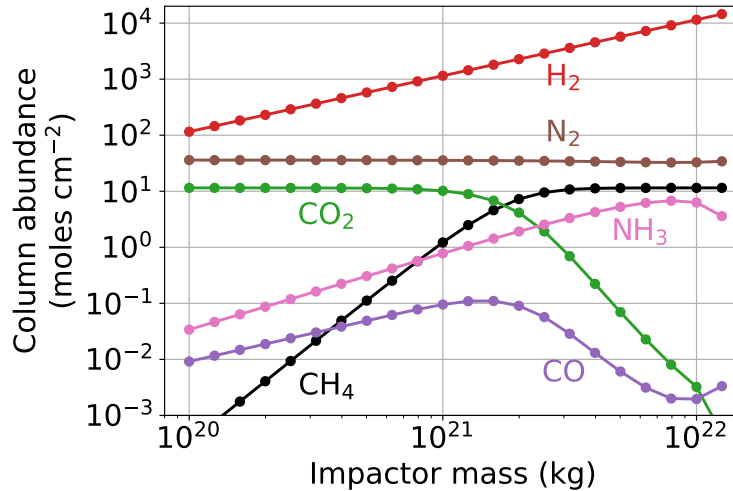
Figure 3 shows our model applied to a  $1.58 \times 10^{21}$  kg ( $\sim 900$  km diameter) impactor. As the steam cools, ammonia quenches when the atmosphere is  $\sim 1200$  K, followed by  $\text{CH}_4$  quenching at  $\sim 950$  K. After quenching, nearly half of the total carbon in the atmosphere exists as  $\text{CH}_4$ . After 4200 years, the steam has largely rained out to form an ocean, leaving behind a  $\text{H}_2$ -dominated atmosphere containing  $\text{CH}_4$  and  $\text{NH}_3$ .  $\text{NH}_3$  is soluble in water, so a fraction should be removed from the atmosphere by dissolution in the newly formed ocean; however our simulations (e.g. Figure 3) do not account for this effect.

Figure 4 shows predicted atmospheric composition at the end of the steam atmosphere (e.g. at 4200 years in Figure 3) as a function of impactor mass. The calculations use gas-phase reactions, and our nominal model parameters (Table 1), including the assumption that 100% of the iron delivered by the impactor reacts with the steam atmosphere to make  $\text{H}_2$ . For example, a  $10^{20}$  kg impactor generates  $1.2 \times 10^2$   $\text{H}_2$  moles  $\text{cm}^{-2}$  which would have a partial pressure of 1.2 bars if the atmosphere did not contain water vapor. A  $10^{22}$  kg impactor generates  $1.1 \times 10^4$   $\text{H}_2$  moles  $\text{cm}^{-2}$  which would have a “dry” partial pressure of 23.8 bars.<sup>2</sup> We find that most of the  $\text{CO}_2$  in the atmosphere is converted to  $\text{CH}_4$  for impactors larger than  $1.6 \times 10^{21}$  kg ( $\sim 900$  km diameter), and that bigger impacts generate more  $\text{NH}_3$ , e.g., a  $10^{22}$  kg impactor makes 0.013 “dry” bars of  $\text{NH}_3$ . Reduced species like  $\text{CH}_4$  and  $\text{NH}_3$  are thermodynamically preferred in the thick  $\text{H}_2$  atmospheres generated by bigger impacts. Large impacts generate big amounts of hydrogen because they deliver more iron which more thoroughly reduces the atmosphere.

The Figure 4 calculations might underestimate the  $\text{CH}_4$  produced in the post-impact atmosphere because they ignore reactions occurring on nickel surfaces that can catalyze  $\text{CH}_4$  generation. If the impactors that struck the Earth during the Hadean resembled enstatite chondrite or carbonaceous chondrite composition then they would have contained 1% - 2% nickel (Lewis 1992, Table 15). This nickel would have coexisted with the rock and iron vapor atmosphere that lasted months to years following a massive impact (Phase 1 in Figure 1). Metals along with silicates would have rained out as spherules covering the entire planet (Genda et al. 2017). As the impact-generated steam cooled, chemical reactions catalyzing  $\text{CH}_4$  production could have occurred on nickel surfaces in the bed of spherules (Schmider et al. 2021). These surface reactions could lower the quench temperature of  $\text{CH}_4$ , causing more of the gas to be produced.

To estimate the effect of nickel catalysis on  $\text{CH}_4$  production, we use our kinetics-climate model box model (Appendix B) with the nickel-surface reaction network developed by Schmider et al. (2021). The network is based on quantum chemistry calculations and about a dozen experiments from the literature. Our micro-kinetics approach is distinct

<sup>2</sup> Partial pressures depend on the mean molecular weight of the atmosphere. The  $10^{22}$  kg simulation in Figure 4 has 65.0 bars  $\text{H}_2$  before ocean vapor condenses, and would have 23.8 bars  $\text{H}_2$  if there was no water vapor in the atmosphere. Both scenarios have the same number of  $\text{H}_2$  molecules in the atmosphere, but have different partial pressures because of dissimilar mean molecular weights. To avoid ambiguity, we occasionally report partial pressures in “dry” bars, which is the partial pressure of a gas if the atmosphere had no water vapor.



**Figure 4.** Predicted atmospheric composition as a function of impactor mass after steam has condensed to an ocean. We use our nominal modeling assumptions (Table 1), and also use gas-phase kinetics. Most  $\text{CO}_2$  is converted to  $\text{CH}_4$  for impactors larger than  $1.6 \times 10^{21}$  kg.

from the empirical one taken by, e.g. [Kress & McKay \(2004\)](#), because our model tries to capture each elementary step of catalysis, rather than use a parameterization that is specific to certain experimental conditions.

Figure 5 shows the quenched methane abundance as a function of impactor mass predicted by our model that includes nickel catalysts. The amount of  $\text{CH}_4$  generated depends strongly on the amount of available nickel surface area. Nickel areas bigger than  $0.1 \text{ cm}^2 \text{ nickel} / \text{cm}^2 \text{ Earth}$  permit more  $\text{CH}_4$  production compared to our gas-phase only model. Assuming a nickel area of  $1000 \text{ cm}^2 \text{ nickel} / \text{cm}^2 \text{ Earth}$ , then a Vesta-size impactor ( $2.6 \times 10^{20}$  kg, 500 km diameter) could convert most  $\text{CO}_2$  in the pre-impact atmosphere to  $\text{CH}_4$ .

Unfortunately, a precise nickel surface area is hard to estimate. The correct value depends on how the rock, iron and nickel spherules mix and precipitate to the surface, and furthermore, how effectively the atmosphere can diffuse through and react on exposed nickel. We do not attempt to compute these effects here, and instead estimate possible upper bounds. Consider a  $2.6 \times 10^{20}$  kg impactor (Vesta-sized) of enstatite chondrite composition, containing 2% by mass Ni ([Lewis 1992](#)). If all this nickel is gathered into 1 mm spheres, a plausible droplet size according to [Genda et al. \(2017\)](#), then the total nickel surface area is  $3.4 \times 10^3 \text{ cm}^2 \text{ nickel} / \text{cm}^2 \text{ Earth}$ . An impactor ten times more massive would deliver ten times more nickel resulting in an upper bound Ni area that is one order of magnitude larger. Significantly smaller nickel particles are conceivable. There is experimental support for the formation of ultra-fine  $< 300 \text{ nm}$  particles in the wake of impacts colliding with an ocean ([Furukawa et al. 2007](#)). For a Vesta-sized impactor, collecting all nickel into 100 nm particles has a nickel area five orders of magnitude large than the 1 mm case -  $3.4 \times 10^9 \text{ cm}^2 \text{ nickel} / \text{cm}^2 \text{ Earth}$ . Overall, the larger nickel areas shown in Figure 5 may be within the realm of possibility.

Figures 4 and 5 optimistically assume that all iron delivered by the impactor reacts with steam to make  $\text{H}_2$ , however, this may not be the case (see Section 3.1). Therefore, in Appendix Figures A2 and A3 we recalculate Figures 4 and 5, but assume that only a fraction of the impactor’s iron reduces the steam atmosphere by extrapolating SPH simulations of impacts (“Model 1B” in Figure 2). The resulting  $\text{H}_2$ ,  $\text{CH}_4$ , and  $\text{NH}_3$  production appear similar, except shifted by a factor of  $\sim 5$  to larger impactors. The results are shifted by this amount because SPH simulations suggest approximately  $\sim 1/5$  of impactor iron is delivered to the atmosphere, while the rest is either embedded in Earth, or ejected to space. We consider these supplementary calculations lower-bounds for impactor generated  $\text{CH}_4$  and  $\text{NH}_3$ .

### 3.3. Phase 3: Long-term photochemical-climate evolution

Several thousand years after a massive impact, the steam-dominated atmosphere would condense to an ocean leaving behind a  $\text{H}_2$ -dominated atmosphere containing  $\text{CH}_4$  and  $\text{NH}_3$  (e.g. at 4200 years in Figure 3). The reducing atmospheric state should persist for millions of years until hydrogen escapes ([Zahnle et al. 2020](#)).

We simulate the long-term evolution of this hydrogen-rich atmosphere using a coupled one-dimensional photochemical-climate model (Appendix C). Figure 6 shows our model applied to the atmosphere following a  $1.58 \times 10^{21}$  kg ( $\sim 900 \text{ km}$  diameter) impactor. We assume a pre-impact atmosphere with 1 bar  $\text{N}_2$  and 0.5 bars of  $\text{CO}_2$ , and sim-

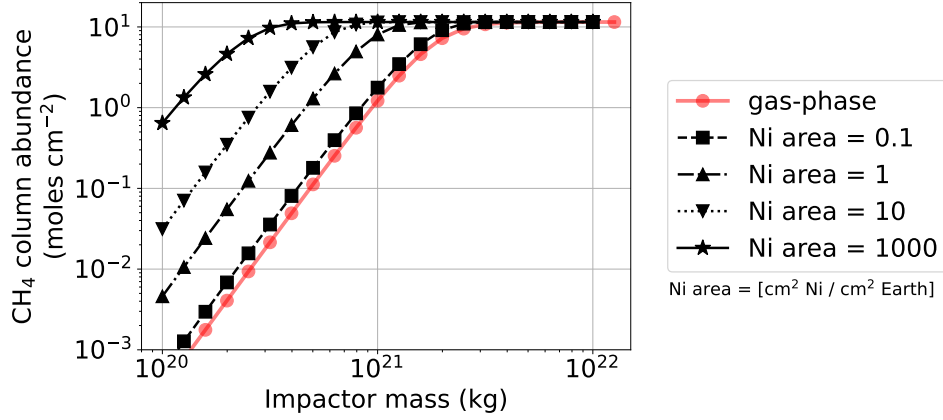


**Figure 5.** The effect of nickel catalysts on post-impact methane production. The calculations use the Table 1 model parameters and the [Schmider et al. \(2021\)](#) surface reaction network. Ni areas larger than  $0.1 \text{ cm}^2 \text{ nickel} / \text{cm}^2 \text{ Earth}$  generates more methane than our model that uses gas-phase reactions, e.g., Figure 4.

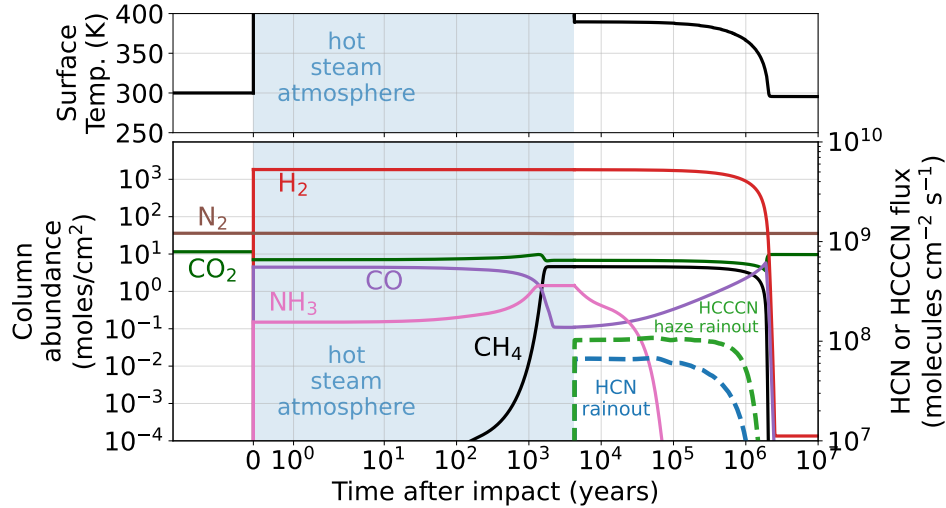


**Figure 6.** Simulated composition and climate of the Hadean atmosphere after a  $1.58 \times 10^{21} \text{ kg}$  impactor that produces 7.0 bars of  $\text{H}_2$  once vaporized ocean water condenses. We use the Table 1 model parameters. The blue shaded region labeled “hot steam atmosphere”, also called Phase 2 in Figure 1, is simulated by the kinetics-climate model described in Appendix B. After this time-period, during Phase 3 of a post-impact atmosphere, we evolve the atmosphere with 1-D photochemical-climate model (Appendix C), which maintains 0.018 bar of  $\text{CH}_4$  between  $4 \times 10^3$  and  $\sim 10^6$  years. Dashed lines are referenced to the right-hand axis. “HCN rainout” is HCN molecules raining out in droplets of water. “HCCCN haze rainout” is the rainout rate of HCCCN incorporated into particles formed from the reaction  $\text{C}_4\text{H} + \text{HCCCN} \rightarrow \text{polymer}$ .  $\text{CH}_4$  and  $\text{N}_2$  photochemistry generates HCN and HCCCN for about one million years until  $\text{H}_2$  escapes to space.

ulate the cooling steam atmosphere with our kinetics-climate climate model (Section 3.2). Next, we use the end of the steam atmosphere simulation as initial conditions for our 1-D photochemical-climate model.

We find that  $\text{N}_2$  and  $\text{CH}_4$  photochemistry generates HCN in a hazy Titan-like atmosphere for about one million years until it is halted by hydrogen escape to space. In this model, the dominant channel producing HCN is  $\text{N} + {}^3\text{CH}_2 \rightarrow \text{HCN} + \text{H}$  where  ${}^3\text{CH}_2$  is ground (triplet) state of the methylene radical derived from methane photolysis. There are two other important paths. The first is  $\text{N} + \text{CH} \rightarrow \text{CN} + \text{H}$  followed by  $\text{H}_2 + \text{CN} \rightarrow \text{HCN} + \text{H}$ , and the second is  $\text{N} + \text{CH}_3 \rightarrow \text{H} + \text{H}_2\text{CN}$  and  $\text{H}_2\text{CN} + \text{H} \rightarrow \text{HCN} + \text{H}_2$ . In all pathways, hydrocarbon radicals (e.g.,  ${}^3\text{CH}_2$  and  $\text{CH}_3$ ) are sourced from photolyzed  $\text{CH}_4$  and atomic N is derived from photolyzed  $\text{N}_2$ , which both occur at high altitudes ( $p < 10^{-5} \text{ bar}$ , Appendix Figure A5). The largest chemical loss of HCN is photolysis followed by  $\text{N} + \text{CN} \rightarrow \text{N}_2 + \text{C}$ .



Other significant losses are paths that form HCCCN aerosols. HCN production and loss in our model is comparable to pathways discussed in similar studies (Zahnle 1986; Tian et al. 2011; Rimmer & Rugheimer 2019).

In Figure 6, HCN mixes to the surface and rains out in droplets of water at a rate of  $\sim 10^7$  molecules  $\text{cm}^{-2} \text{s}^{-1}$ . HCN also dissolves into the ocean at a similar rate, where we assume it is eventually destroyed by hydrolysis (not shown in Figure 6). To emulate HCN dissolution and destruction in the ocean, we assume a  $7 \times 10^{-3} \text{ cm s}^{-1}$  deposition velocity justified in Appendix C.4. Additionally, a relatively small amount of HCN polymerizes to haze particles in our model via  $\text{H}_2\text{CN} + \text{HCN} \rightarrow \text{polymer}$  following Lavvas et al. (2008a), which falls and rains out in water droplets to the surface.

Our results differ from the simulations of Zahnle et al. (2020), which suggested that the duration of HCN production after an impact was limited by rapid photolysis of methane. The Figure 6 simulation finds that the  $\text{CH}_4$  lifetime is 4.8 million years because, following photolysis,  $\text{CH}_4$  efficiently recombines in a hydrogen rich atmosphere from the following reaction, which is well known in the atmospheres of the giant planets in our solar system (Appendix Figure A4).



Zahnle et al. (2020) did not account for Reaction 3. The lifetime of cyanide production is therefore instead determined by the timescale of hydrogen escape to space. Significant hydrogen escape permits the destruction of most atmospheric  $\text{CH}_4$  because Reaction 3 becomes inefficient, which in turn ceases  $\text{CH}_4$ -driven HCN production.

In Figure 6, HCCCN is primarily destroyed by photolysis and produced by the following reaction from acetylene and the cyanide radical,



A fraction of produced HCCCN reacts to form aerosols via  $\text{C}_4\text{H} + \text{HCCCN} \rightarrow \text{polymer}$  following Lavvas et al. (2008a). These polymers fall and mix toward the surface where they rain out in droplets of water at a rate of  $\sim 10^8$  molecules  $\text{cm}^{-2} \text{s}^{-1}$ . Most gas-phase HCCCN is either destroyed by photolysis or incorporated into aerosols, causing vanishingly small surface HCCCN gas pressures ( $< 10^{-16}$  bar).

In Figure 6, impact-generated ammonia persists for nearly  $10^5$  years.  $\text{NH}_3$  is primarily destroyed by photolysis, but then recombines from reactions with hydrogen:



Reactions 5 and 6 are relatively efficient in a hydrogen-rich atmosphere. Ammonia photolysis primarily occurs at the  $10^{-3}$  bar altitude, while haze is largely produced above the  $10^{-5}$  bar altitude. Therefore, haze particles partially shield ammonia from photolysis, extending the  $\text{NH}_3$  lifetime (Sagan & Chyba 1997). Our model assumes the haze particles are perfect spheres with optical properties governed by Mie theory. Observations of Titan's haze have revealed that hydrocarbon haze particles have a fractal structure which absorb and scatter UV more effectively than Mie spheres (Wolf & Toon 2010). Therefore, our model likely overestimates  $\text{NH}_3$  photolysis in post-impact atmospheres.

Figure 6 assumes that all  $\text{NH}_3$  is in the atmosphere and that it does not rain out, but the gas is highly soluble in water and should dissolve in the ocean where it hydrolyzes to ammonium,  $\text{NH}_4^+$ . Zahnle et al. (2020) showed that  $\text{NH}_3$  partitioning between the atmosphere and ocean depends on ocean temperature and pH. For an atmosphere with 1.56 bars of total  $\text{NH}_3$  and a 373 K ocean at pH = 7.8, Zahnle et al. (2020) finds that  $\sim 1\%$  of  $\text{NH}_3$  would persist in the atmosphere, while the rest is dissolved in the ocean. Ammonia dissolution in the ocean would protect it from photolysis perhaps lengthening the lifetime of ammonia in the atmosphere-ocean system. Overall, since our model neglects  $\text{NH}_3$  ocean dissolution and likely overestimates  $\text{NH}_3$  photolysis, then we probably underestimate the lifetime of  $\text{NH}_3$  in Figure 6.

While HCN and HCCCN are produced in Figure 6, the surface temperature would be  $\sim 390$  K primarily caused by  $\text{H}_2$ - $\text{H}_2$  collision-induced absorption (CIA), which has a significant greenhouse effect in thick  $\text{H}_2$  atmospheres like this one of 8.5 bars total pressure. The atmosphere cools to  $\sim 300$  K after  $\text{H}_2$  escapes to space.

Figure 7 applies our model to various impactor masses. The results show the Hadean atmosphere 10,000 years after the post-impact generated steam atmosphere has condensed to an ocean. We choose 10,000 years after ocean

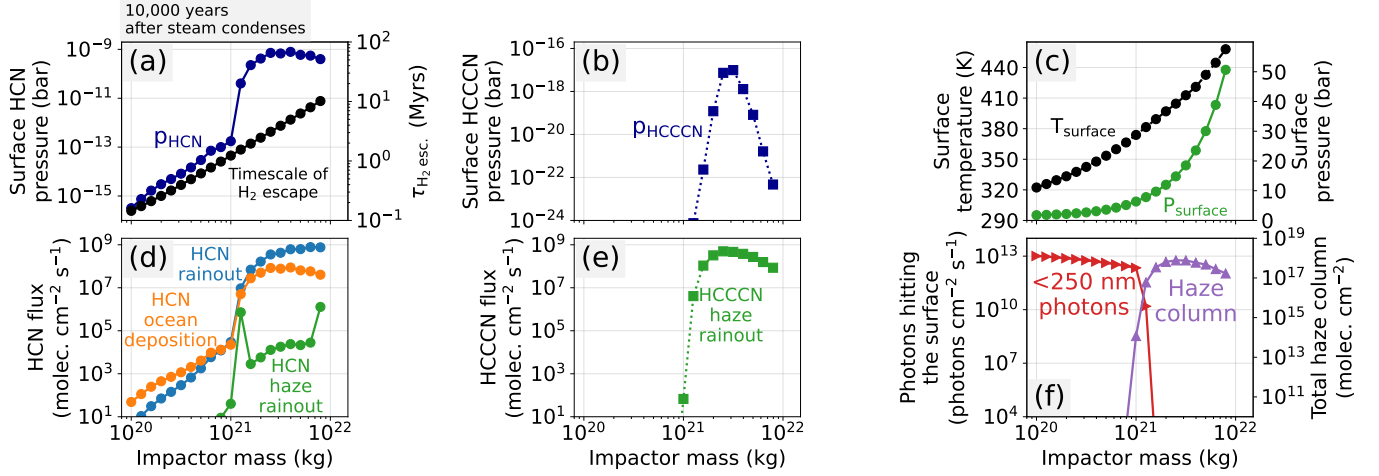


**Figure 7.** The state of the Hadean post-impact atmospheres 10,000 years after steam condenses to an ocean. This time period is within Phase 3 of a post-impact atmosphere indicated in Figure 1. The simulations assume the Table 1 parameters and gas-phase reactions during the cooling steam atmosphere. (a) The surface HCN pressure and timescale of  $H_2$  escape, which can be interpreted as the approximate duration of HCN and HCCCN production. (b) The HCCCN surface pressure. (c) The surface temperature and pressure. (d) The HCN deposition rate in the ocean and the rate HCN leaves the atmosphere in rain drops. “HCN haze rainout” is the rainout rate of an aerosol created via the reaction  $H_2CN + HCN \rightarrow \text{polymer}$ . (e) The rainout rate of an aerosol formed from the reaction  $C_4H + HCCCN \rightarrow \text{polymer}$ . (f) The  $< 250$  nm photons hitting the surface, and the total hydrocarbon haze column abundance. Impactors larger than  $10^{21}$  kg produce haze-rich atmospheres and a stepwise increase in HCN and HCCCN production.

condensation because this is adequate time for the atmosphere to reach a quasi-photochemical steady-state that does not change significantly until hydrogen escapes (e.g. Figure 6). Figure 7d and 7e show a sharp increase in the HCN and HCCCN production for impactors larger than  $10^{21}$  kg ( $\sim 780$  km). Such large impacts generate  $CH_4/CO_2 > 0.1$  (Figure 4), which makes a thick Titan-like haze (Trainer et al. 2006). Haze shielding causes  $CH_4$  photolysis to be higher in the atmosphere and closer to  $N_2$  photolysis, therefore the photolysis products of both species can more efficiently combine to make cyanides (Appendix Figure A5). Additionally, HCCCN production requires acetylene (Reaction 4), which is a haze precursor that accumulates when  $CH_4/CO_2 > 0.1$ . These Titan-like atmospheres have  $\sim 10^{-9}$  bar surface HCN, and HCN ocean deposition and rainout rates between  $10^7$  and  $10^9$  HCN molecules  $cm^{-2} s^{-1}$  persisting on hydrogen escape timescales ( $> 1$  million years). HCCCN is incorporated into aerosols before raining out to the surface at a rate of up to  $10^9$  HCCCN molecules  $cm^{-2} s^{-1}$ .

In addition to photochemistry, lightning should also generate HCN (Chameides & Walker 1981; Stribling & Miller 1987). Appendix Figure A8 shows HCN production from lightning for the same time period as the Figure 7 simulation using methods described in Chameides & Walker (1981). Assuming the same lightning dissipation rate as modern Earth’s, we find that lightning produces up to  $\sim 10^4$  HCN molecules  $cm^{-2} s^{-1}$ . This value is small compared to the  $10^7 - 10^9$  HCN molecules  $cm^{-2} s^{-1}$  produced from photochemistry after  $> 10^{21}$  kg impacts.

Larger impacts generate a thicker  $H_2$  atmosphere which make the atmosphere warmer (Figure 7c). For impactors  $> 10^{21}$  kg, which generate substantial HCN and HCCCN, the surface temperature is  $> 380$  K. Figure 7f shows that impactors that produce substantial haze shield the surface from  $< 250$  nm photons, which means that prebiotic schemes that require high energy UV light (e.g., Patel et al. 2015) would need to rely on stockpiling of the nitriles for later use.

The Hadean Earth  $CO_2$  concentration is uncertain. Models of the Hadean geologic carbon cycle argue for  $CO_2$  levels between  $\sim 10^{-5}$  and 1 bar at 4 Ga with a median value of  $\sim 0.5$  bar and a 95% uncertainty spanning  $10^{-5}$  to 1 bar (Kadoya et al. 2020). However, these values might be unrealistically small because a large impact would warm surface rocks possibly causing carbonates to degass thereby increasing the atmospheric  $CO_2$  reservoir. Up to  $\sim 80$  bars of  $CO_2$  may potentially be liberated from surface carbonates (Krissansen-Totton et al. 2021).

Figure 8 explores the effect of different pre-impact  $CO_2$  abundances on HCN and HCCCN production in post-impact atmospheres. The simulations are snapshots of the atmosphere 10,000 years after the impact-vaporized steam has condensed to an ocean. Larger pre-impact  $CO_2$  causes larger HCN and HCCCN production because it allows more  $CH_4$  to form in the cooling steam atmosphere. As discussed previously,  $CH_4$  is closely tied to photochemical

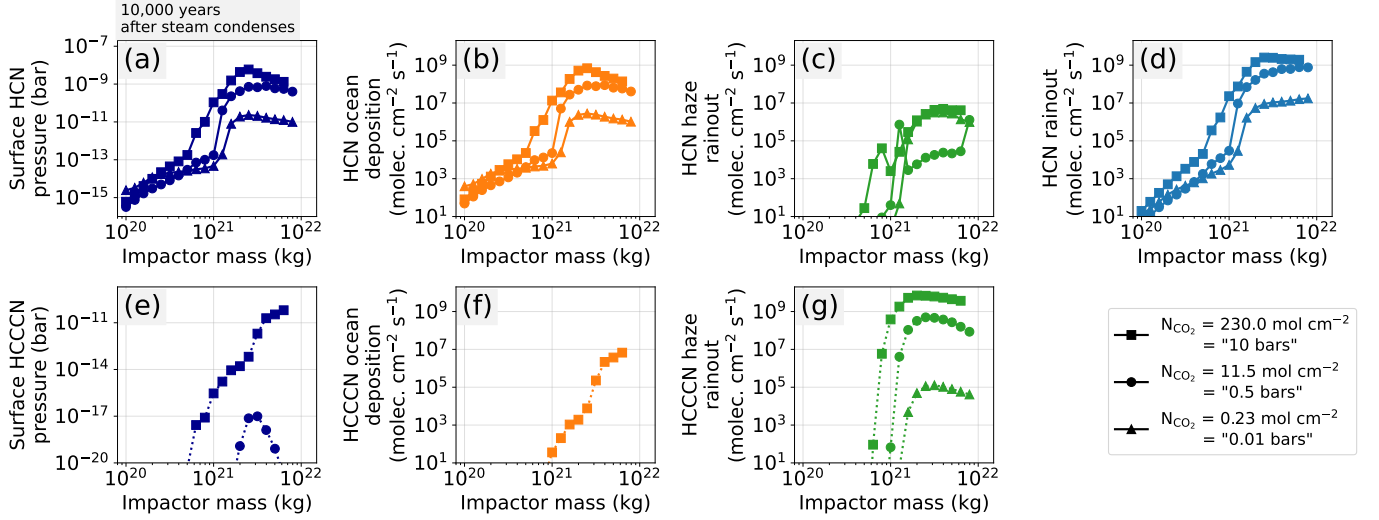


**Figure 8.** The effect of the pre-impact  $\text{CO}_2$  abundance on HCN and HCCCN production in post-impact atmospheres. All values are for the atmosphere 10,000 years after the steam condenses to an ocean, which is within Phase 3 of a post-impact atmosphere (Figure 1). The simulations assume the Table 1 parameters, except vary the pre-impact  $\text{CO}_2$  inventory between 0.01 bar (triangles), 0.5 bar (circles), and 10 bars (squares). The calculations use gas-phase chemistry during the cooling steam atmosphere. Panels (a) - (d) show the surface HCN abundance and fluxes, while (e) - (g) show HCCCN production. Our model assumes that HCCCN is not soluble in water and does not rainout, therefore we omit a panel showing HCCCN rainout. Prebiotic nitrile production is directly correlated with the pre-impact  $\text{CO}_2$  inventory.

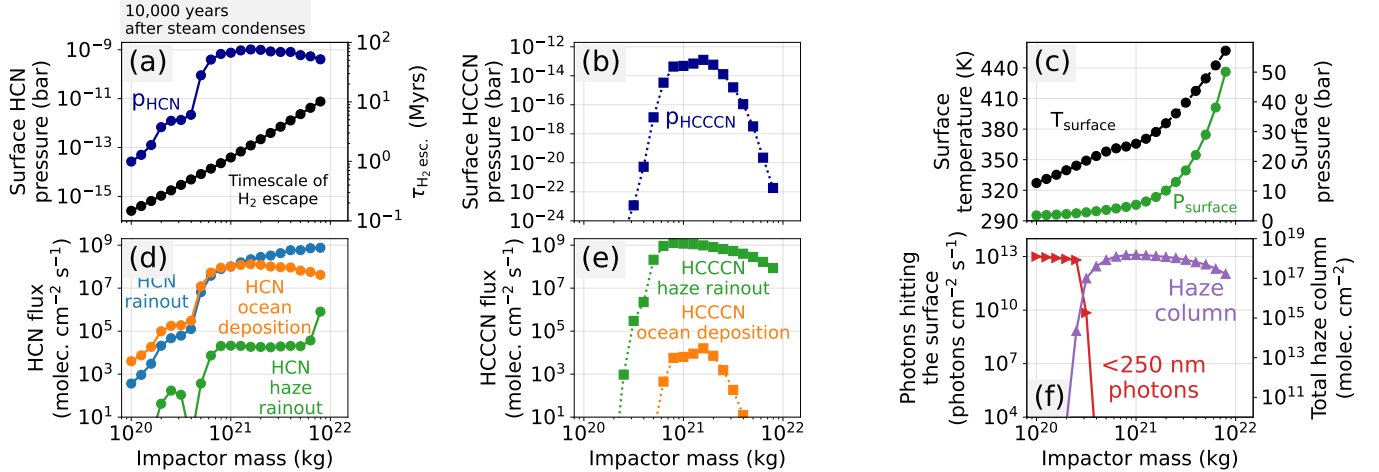


**Figure 9.** Identical to Figure 7, except simulations account for nickel-surface reactions which catalyze methane production as the steam atmosphere cools (Schmider et al. 2021). We assume a nickel surface area of  $10 \text{ cm}^2 \text{ nickel} / \text{cm}^2 \text{ Earth}$  (for context, see Figure 5). Nickel catalysts cause more efficient  $\text{CH}_4$  generation, permitting bigger HCN and HCCCN production for smaller impactors compared to the gas-phase only scenario (Figure 7).

cyanide generation. Regardless of the pre-impact  $\text{CO}_2$  concentrations, HCN and HCCCN production sharply increases for impactors larger than  $\sim 10^{21} \text{ kg}$  due to more efficient haze production (Figure 7, and corresponding text).

Figure 9 shows the state of the atmosphere after impacts of various size assuming  $10 \text{ cm}^2 \text{ nickel} / \text{cm}^2 \text{ Earth}$  is present in the steam atmosphere to catalyze methane production. The nickel causes more efficient conversion of  $\text{CO}_2$  to  $\text{CH}_4$  compared to the gas-phase only scenario (Figure 7) permitting bigger HCN and HCCCN production for smaller impactors. For example, a  $5 \times 10^{20} \text{ kg}$  ( $\sim 610 \text{ km}$ ) impactor which accounts for nickel catalysts (Figure 9) has comparable HCN and HCCCN production to a  $1.6 \times 10^{21} \text{ kg}$  ( $\sim 900 \text{ km}$  diameter) impactor if no nickel catalysts are assumed in the cooling steam atmosphere (Figure 7).

A critical assumption in this section is that 100% of the iron delivered by impactors reacts with steam to generate  $\text{H}_2$ . As discussed in Section 3.1, it is possible that the post-impact atmosphere is less thoroughly reduced by impactor iron. Appendix Figures A6 and A7 recalculate main text Figures 7 and 9, assuming that a fraction (approximately 15% to 30%) of impactor iron reduces the steam atmosphere based on SPH simulations (“Model 1B” in Figure 2). This alternative assumption requires that impactors  $\sim 5$  times more massive are required to generate a haze-rich post-impact atmosphere with copious HCN and HCCCN production. For example, in Figure 7, recall that there is a sharp increase in cyanide production for impactors larger than  $10^{21}$  kg ( $\sim 780$  km). Appendix Figure A6, which instead assumes a fraction of iron reduces the steam atmosphere, finds that the sharp increase in cyanide production occurs for impacts larger than  $5 \times 10^{21}$  kg ( $\sim 1330$  km). However, the presence of nickel catalysts may permit large prebiotic nitrile production for smaller impactors, even under pessimistic post-impact  $\text{H}_2$  generation (Appendix Figure A7).

## 4. DISCUSSION

### 4.1. Comparison to previous work

Recently, Zahnle et al. (2020) performed calculations of post-impact atmospheres using simpler models than the ones used in this article. Our results differ in several important ways. First, we find that our purely gas-phase model of the post-impact steam atmosphere (Section 3.2) predicts less  $\text{CH}_4$  generation than the model used in Zahnle et al. (2020). For example, Figure 4 predicts that most  $\text{CO}_2$  is converted to  $\text{CH}_4$  for impactors larger than  $1.6 \times 10^{21}$  kg. Figure 2 (top panel) in Zahnle et al. (2020), which is a comparable scenario, suggests a  $5 \times 10^{20}$  kg impactor is required to convert most of the atmospheric  $\text{CO}_2$  to  $\text{CH}_4$ . The difference is likely caused by different approaches to computing  $\text{CH}_4$  quenching, or freeze-out, as the atmosphere cools. Our kinetics-climate model automatically computes  $\text{CH}_4$  quenching by tracking the elementary reactions producing and destroying  $\text{CH}_4$  along with many other atmospheric species. In most of our simulations of cooling post-impact atmospheres,  $\text{CH}_4$  quenches when the temperature is between 900 and 1000 K. Zahnle et al. (2020) instead used equilibrium chemistry modeling with a parameterization for  $\text{CH}_4$  quenching derived from kinetics calculations of  $\text{H}_2$ -dominated brown dwarf atmospheres (Zahnle & Marley 2014). This parameterization predicts  $\sim 800$  K  $\text{CH}_4$  quenching temperatures. The different quenching temperatures between our model and the Zahnle et al. (2020) model suggests that the Zahnle et al. (2020) kinetics parameterization is likely not suitable for a cooling steam-rich atmosphere.

The new photochemical model predicts longer post-impact  $\text{CH}_4$  lifetimes than the Zahnle et al. (2020) model. As mentioned previously, Zahnle et al. (2020) included  $\text{CH}_4$  photolysis, but neglected Reaction 3, which efficiently recombine photolysis products in hydrogen-rich atmospheres. In our model, these recombination reactions allow  $\text{CH}_4$  to persist in most post-impact atmospheres until hydrogen escapes to space ( $\sim$  millions of years). Zahnle et al. (2020) instead finds that  $\text{CH}_4$  is eradicated from the atmosphere before hydrogen escape.

Finally, nitrile production and rainout in our new model depend strongly on the presence of haze and the  $\text{CH}_4/\text{CO}_2$  ratio, which was not the case in Zahnle et al. (2020). Our model finds that up to  $\sim 10^9$  molecules  $\text{cm}^{-2} \text{s}^{-1}$  HCN and HCCCN is rained out in hazy post-impact atmospheres with  $\text{CH}_4/\text{CO}_2 > 0.1$  (Figure 7). When  $\text{CH}_4/\text{CO}_2 < 0.1$ , there is little haze, and HCN production is  $< \sim 10^5$  molecules  $\text{cm}^{-2} \text{s}^{-1}$  and HCCCN production is negligible. Haze causes  $\text{CH}_4$  and  $\text{N}_2$  photolysis products to be close in altitude so that they efficiently react to make cyanides (Appendix Figure A5). Additionally, HCCCN generation requires  $\text{C}_2\text{H}_2$  in our model (Reaction 4), which is only abundant in hazy atmospheres. In contrast, Zahnle et al. (2020) finds that cyanide production rate in post-impact atmospheres is  $10^8$  to  $10^{10}$  molecules  $\text{cm}^{-2} \text{s}^{-1}$  regardless of the presence of haze and the  $\text{CH}_4/\text{CO}_2$  ratio. Our results differ largely because our model is 1-D (has vertical transport), while the Zahnle et al. (2020) is a zero dimensional box model. HCN production depends on the proximity of  $\text{CH}_4$  and  $\text{N}_2$  photolysis, but a box model cannot account for this 1-D effect. Furthermore, Zahnle et al. (2020) does not distinguish between different prebiotic nitriles (e.g. HCN and HCCCN), or determine their surface concentrations and rainout rates. Also, Zahnle et al. (2020) does not have a coupled climate model.

Cometary and lightning sources of HCN are relatively small compared to our estimated photochemical production rates in haze-rich post-impact atmospheres. Todd & Öberg (2020) calculated that comets could deliver  $\sim 1.8 \times 10^5$  HCN molecules  $\text{cm}^{-2} \text{s}^{-1}$  to the Hadean Earth, a value  $\sim 4$  orders of magnitude smaller than HCN from photochemistry in our most optimistic models. As discussed in Section 3.3, we find that HCN production from lightning in post-impact atmospheres to be at most  $\sim 10^4$  HCN molecules  $\text{cm}^{-2} \text{s}^{-1}$  which is also small compared to UV photochemistry in

a CH<sub>4</sub> rich atmosphere. This result agrees with [Pearce et al. \(2022\)](#), who also finds that lightning-produced HCN is relatively insignificant.

[Rimmer & Shorttle \(2019\)](#) suggested that localized ultra-reducing magma rich in carbon and nitrogen might outgas HCN and HCCCN. They imagine this gas interacting with subsurface water causing high concentrations of dissolved prebiotic molecules, and therefore a setting for origin of life chemistry. While this idea may have merit, their calculations do not account for graphite saturation in magma, which may inhibit outgassing of reduced carbon-bearing species, like HCN ([Hirschmann & Withers 2008](#); [Wogan et al. 2020](#); [Thompson et al. 2022](#)). Additionally, [Rimmer & Shorttle \(2019\)](#) did not self-consistently account for the solubility of gases in magma, which has been hypothesized to prevent the outgassing of H-bearing gases, like CH<sub>4</sub> or HCN ([Wogan et al. 2020](#)). Therefore, we argue that a hypothesized volcanic source of HCN and HCCCN requires further modeling and experiments before it can be compared to a photochemical source, but, in general, seems challenging.

#### 4.2. Origin of life setting and stockpiling of cyanides

The Hadean Earth may have had less land but was likely speckled with hot-spot volcanic islands similar to modern-day Hawaii ([Bada & Korenaga 2018](#)), and possibly had continental land ([Korenaga 2021](#)) where nitriles could accumulate. The majority of HCCCN and HCN produced in post-impact atmospheres would dissolve or rainout into the ocean where it would be diluted and gradually removed by hydrolysis reactions ([Miyakawa et al. 2002](#)) or complexation with dissolved ferrous iron ([Keefe & Miller 1996](#)). However, some of the nitriles would be deposited in lakes or ponds on land. We consider, first, equilibrium with atmospheric  $p_{\text{HCN}}$  and, second, time-integrated deposition.

Nitrile concentrations in waterbodies on land in equilibrium with the atmosphere according to Henry’s law would be too small to participate in prebiotic schemes that form ribonucleotides. Our models predict HCN surface pressures up to  $10^{-9}$  bar (Figure 7). For a warm 373 K pond, Henry’s law predicts the dissolved HCN concentration is  $4 \times 10^{-11}$  mol L<sup>-1</sup>. Yet,  $\sim 0.01$  mol L<sup>-1</sup> HCN is required for polymerization ([Sanchez et al. 1967](#)) and published prebiotic schemes can use 1 mol L<sup>-1</sup> HCN ([Patel et al. 2015](#)).

Additionally, while nitriles are produced in post-impact atmospheres, waterbodies on land would likely be too warm for prebiotic chemistry. In the Figure 6 simulation, substantial HCN and HCCCN production occurs in the aftermath of big impacts when the surface temperature is  $\sim 390$  K caused by a H<sub>2</sub>-H<sub>2</sub> CIA greenhouse. Nickel catalysts permit big HCN and HCCCN production for surface temperatures as small as  $\sim 360$  K (Figure 9). Nucleotide building blocks are fragile at such hot temperatures and conditions may not be conducive to an RNA world ([Bada & Lazcano 2002](#)).

We propose that cyanides produced in hot post-impact atmospheres may instead be preserved, stockpiled, and concentrated, and used in prebiotic schemes at a later time when the climate is colder. Cyanide rainout and stockpiling could occur for millions of years until HCN production is halted by H<sub>2</sub> escape to space (Figure 6). Once H<sub>2</sub> escapes, the surface temperature would drop to  $\sim 300$  K (Figure 6), and over longer timescales the carbonate-silicate cycle might settle on even colder climates because impact ejecta promotes CO<sub>2</sub> sequestration ([Kadoya et al. 2020](#)). In this cold climate, cyanide stockpiled into salts could be released as HCN or CN<sup>-</sup> into water bodies on land because of rehydration, volcanic or impact heating ([Patel et al. 2015](#); [Sasselov et al. 2020](#)), or UV exposure ([Todd et al. 2022](#)). Liberation of cyanide could enable the prebiotic schemes that make RNA.

[Toner & Catling \(2019\)](#) investigated a mechanism for stockpiling cyanides. Their thermodynamic calculations show that HCN can be preserved as ferrocyanide salts in evaporating carbonate-rich lakes. However, the [Toner & Catling \(2019\)](#) numerical experiments were at 273 K and 298 K, which are far colder environments than the  $> 360$  K surface temperatures that coincide with large HCN production in post-impact atmospheres (Figure 9). Although, [Toner & Catling \(2019\)](#) did not address stockpiling of HCCCN, cyanoacetylene can be captured by 4,5-Dicyanoimidazole (DCI), a byproduct of adenine synthesis, to make crystals of 4,5-dicyanoimidazole (CV-DCI) ([Ritson et al. 2022](#)) and it is possible that other capture mechanisms are yet to be discovered. Overall, the feasibility of stockpiling prebiotic nitriles in post-impact conditions requires further geochemical modeling and experiments.

#### 4.3. Impactor size and the likelihood of the origin of life

We hypothesize that CH<sub>4</sub>/CO<sub>2</sub>  $> 0.1$  might be an important threshold required for a post-impact atmosphere to produce useful concentrations of nitriles for origin of life chemistry. Figure 10 shows HCN and HCCCN haze rainout as a function of the atmospheric CH<sub>4</sub>/CO<sub>2</sub> mole ratio for every post-impact simulation in this article. When CH<sub>4</sub>/CO<sub>2</sub>  $> 0.1$ , the atmosphere is hazy, and HCN and HCCCN are delivered to the surface at a rate of up to  $\sim 10^9$  molecules cm<sup>-2</sup> s<sup>-1</sup>. In contrast, atmospheres with CH<sub>4</sub>/CO<sub>2</sub>  $< 0.1$  rainout less than  $10^5$  HCN molecules



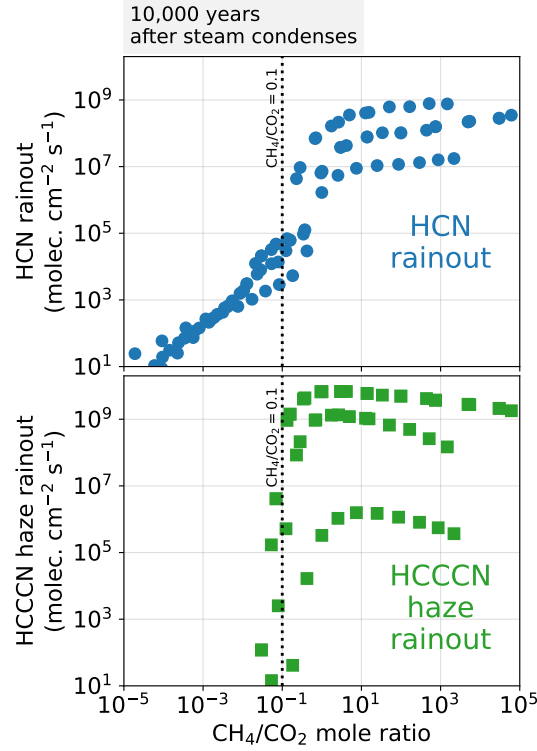


**Figure 10.** HCN rainout and HCCCN haze rainout as a function of the  $\text{CH}_4/\text{CO}_2$  mole ratio in all simulated post-impact atmospheres. The figure considers simulations shown in Figure 7, 8, 9, A6 and A7. All values are for the atmosphere 10,000 years after steam has condensed to an ocean. The HCN and HCCCN haze production is significantly larger for atmospheres with  $\text{CH}_4/\text{CO}_2 \gtrsim 0.1$ .

$\text{cm}^{-2} \text{s}^{-1}$  and have surface HCN concentrations less than  $10^{-13}$  bar (Figure 7). Such small HCN concentrations may be challenging to stockpile as ferrocyanides (Toner & Catling 2019). Additionally, modeled atmospheres with  $\text{CH}_4/\text{CO}_2 < 0.1$  produce negligible HCCCN, yet the molecule is required in prebiotic schemes to synthesize pyrimidine (cytosine and uracil) nucleobase precursors to RNA (Powner et al. 2009; Okamura et al. 2019; Becker et al. 2019).

The impactor mass required to generate an atmosphere with  $\text{CH}_4/\text{CO}_2 > 0.1$  is uncertain. Our optimistic model, which considers the effect of nickel-catalyzed methane production, requires a  $> 4 \times 10^{20}$  kg ( $> 570$  km) impactor (Figure 9). The lunar cratering record and abundance of highly siderophile elements Earth’s mantle imply that between 4 and 7 such impacts occurred during the Hadean (Marchi et al. 2014; Zahnle et al. 2020). Our least optimistic model needs a  $> 5 \times 10^{21}$  kg ( $> 1330$  km) impact to create a post-impact atmosphere with  $\text{CH}_4/\text{CO}_2 > 0.1$  because it assumes only a fraction of iron delivered to Earth reacts with the ocean to create atmospheric  $\text{H}_2$  (Appendix Figure A6). The Hadean only experienced 0 to 2 collisions this large (Zahnle et al. 2020). The precise minimum impactor mass to make an atmosphere with  $\text{CH}_4/\text{CO}_2 > 0.1$  depends on the importance of atmospheric equilibration with a melt pond (Section 3.1, and Itcovitz et al. (2022)), the fraction of impactor iron that reduces the atmosphere, and the effect of Nickel and other surface catalysts on  $\text{CH}_4$  kinetics.

An additional consideration is that any progress toward the origin of life caused by an impact could be erased by a subsequent impact that sterilizes the planet. For example, suppose a  $> 500$  km impact that vaporizes the ocean sterilizes the globe (Citron & Stewart 2022). With our most pessimistic calculations for post-impact  $\text{CH}_4$  generation a  $> 1330$  km ( $> 5 \times 10^{21}$  kg) impact is required to create an atmosphere that generates significant HCN and HCCCN. In this scenario, the last  $> 1330$  km impact favorable for prebiotic chemistry would likely be followed by a 500 to 1330 km impact that would destroy any primitive life without rekindling it. Alternatively, our optimistic model for post-impact  $\text{CH}_4$  generation only requires a  $> 4 \times 10^{20}$  kg ( $> 570$  km) impact to create an atmosphere with  $\text{CH}_4/\text{CO}_2 > 0.1$ . In this case, the final  $> 570$  km impact that might kickstart the origin of life is unlikely to be followed by a slightly smaller 500 km to 570 km sterilizing impact.



A caveat to the reasoning in the previous paragraph is that ocean-vaporization may not have sterilized the planet because microbes could have possibly survived in the deep subsurface (Sleep et al. 1989; Grimm & Marchi 2018).

In summary, we suggest that  $\text{CH}_4/\text{CO}_2 > 0.1$  may be an important threshold for post-impact atmospheres to be conducive to the origin of life because they generate  $> 4$  orders of magnitude larger surface HCN concentrations, and are the only modeled atmospheres capable of generating HCCCN. We find that the minimum impactor mass required to create a post-impact atmosphere with  $\text{CH}_4/\text{CO}_2 > 0.1$  is between  $4 \times 10^{20}$  and  $5 \times 10^{21}$  kg (570 to 1330 km). The value is uncertain because we do not know how effectively iron delivered by an impact reduces the atmosphere (Section 3.1), the importance of atmospheric equilibration with a melt pond (Section 3.1), and because it is hard to estimate a realistic surface area of nickel catalysts available during the cooling steam atmosphere (Section 3.2).

#### 4.4. Model caveats and uncertainties

Perhaps the most significant caveat to the modeling effort described above is that we did not consider  $\text{H}_2$  from reactions between a hot post-impact atmosphere and solid, non-melted crust. Section 3.1 explores impact  $\text{H}_2$  made by two mechanisms: (1) reduction of the atmosphere by impact-derived iron and (2) atmospheric equilibration with a melt pond made by the impact. However, it is also conceivable that while the atmosphere is hot and steam-rich in the  $\sim 10^3$  years following an impact (i.e. Phase 2), water vapor could permeate through and react with the solid crust to produce  $\text{H}_2$  by a process like serpentinization. Specifically,  $\text{H}_2\text{O}$  reduction by FeO in the solid crust could make  $\text{H}_2$ :



In our nominal model (Figure 4 and 7), we require a post-impact atmosphere has  $> 2 \times 10^3 \text{ H}_2 \text{ mol cm}^{-2}$  (i.e. the equivalent of converting 13% of Earth’s ocean to  $\text{H}_2$ ) in order to reach a  $\text{CH}_4/\text{CO}_2 > 0.1$  and big nitrile production rates. Assuming a crustal FeO content of 8 wt% (Takahashi 1986), then  $2 \times 10^3 \text{ H}_2 \text{ mol cm}^{-2}$  could be produced by reacting water with FeO in the top  $\sim 16$  km of Earth’s lithosphere. The feasibility of extensive water-rock  $\text{H}_2$  generation depends on the permeability of the crust and the pressure gradients driving subsurface fluid circulation. For example, low permeability rocks with slow water circulation may not permit serpentinization of the upper crust within  $\sim 10^3$  years while the atmosphere is hot and steam-rich. A comprehensive model is out of the scope of this article, but if attainable, significant water-rock reactions might produce a thick  $\text{H}_2$  atmosphere after relatively small impacts (e.g.  $10^{20}$  kg) which favors a  $\text{CH}_4/\text{CO}_2 > 0.1$  and significant nitrile generation.

Another possibility, which we do not investigate in detail, is that atmosphere-crust reactions occur in the immediate aftermath of a giant impact (i.e. Phase 1), rather than over  $\sim 10^3$  as previously discussed. A large impact could produce a global ejecta blanket several kilometers thick of mixed hot water and rock. As water was vaporized to form a steam atmosphere, the water and rock slurry could chemically equilibrate, producing  $\text{H}_2$ .

Zahnle et al. (2020) attempted to account for atmosphere-crust interaction by equilibrating the post-impact steam atmosphere (Phase 2) to a mineral redox buffer. For example, their Figure 5 assumes the atmosphere has a fixed oxygen fugacity set by the FMQ buffer at an assumed 650 K methane quench temperature. The calculation predicts most  $\text{CO}_2$  is converted to  $\text{CH}_4$  for impacts as small as  $\sim 5 \times 10^{19}$  kg, but Zahnle et al. (2020) did not determine whether such significant atmosphere-crust interaction is physically plausible.

An additional shortcoming is that our climate model is relatively simple. Throughout the Results section, our climate code assumes an isothermal 200 K stratosphere, a saturated adiabatic troposphere (i.e. relative humidity,  $\phi = 1.0$ ), and ignores clouds. However, many of our simulated post-impact atmospheres contain a hydrocarbon haze which should absorb sunlight and warm the stratosphere (Arney et al. 2016). Also, in a hydrogen-dominated atmosphere, water vapor has a larger molecular weight compared to the background gas which could inhibit convection (Leconte et al. 2017) and perhaps cause low relative humidities. Furthermore, low-altitude clouds reflect sunlight and should cool a planet while high clouds have a greenhouse warming effect (Goldblatt & Zahnle 2011).

Figure 11 attempts to show the uncertainty in our climate calculations as a function of three free parameters: stratosphere temperature, relative humidity, and low-altitude clouds which we crudely approximate by varying the surface albedo. The calculation uses the composition of the atmosphere after a  $5 \times 10^{20}$  kg impact in Figure 9 immediately after the steam atmosphere has condensed to an ocean. Our nominal climate parameters ( $T_{\text{strat}} = 200$  K,  $\phi = 1$ ,  $A_s = 0.2$ ) predict a 361 K surface temperature. A warm stratosphere caused by hydrocarbon UV absorption and high albedo surface clouds might cause the surface to be  $\sim 30$  K colder than our nominal model, assuming water vapor is saturated. On the other hand, low relative humidities, which might be favored in convection-inhibited  $\text{H}_2$  dominated atmospheres, flatten the troposphere adiabat which warms the surface (Leconte et al. 2017). While Figure

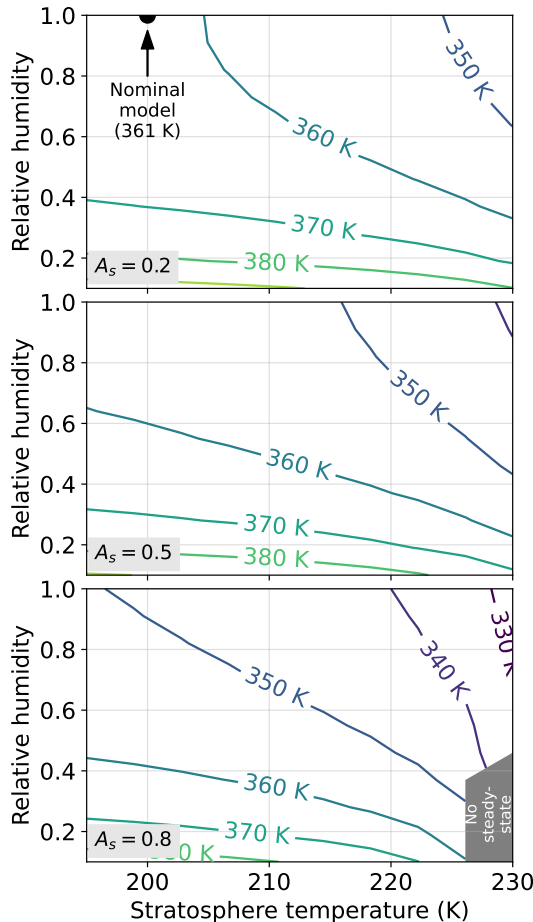


**Figure 11.** Surface temperature of a post-impact atmosphere as a function of stratosphere temperature, relative humidity, and surface clouds which we crudely approximate with the surface albedo ( $A_b$ ). The atmosphere has  $5.9 \text{ mol cm}^{-2} \text{ CO}_2$ ,  $5.6 \text{ mol cm}^{-2} \text{ CH}_4$ ,  $36 \text{ mol cm}^{-2} \text{ N}_2$ ,  $557 \text{ mol cm}^{-2} \text{ H}_2$ ,  $0.01 \text{ mol cm}^{-2} \text{ CO}$ , and a liquid water ocean at the surface. This is the same composition of the atmosphere after a  $5 \times 10^{20} \text{ kg}$  impact in Figure 9 once steam has condensed to an ocean. The gray shaded region labeled “no steady-state” has no steady-state climate solutions that balance incoming shortwave and outgoing longwave energy. Uncertainties in our assumed stratosphere temperature, relative humidity and the effects of low-altitude clouds predict surface temperatures from  $\sim 330 \text{ K}$  to  $\sim 390 \text{ K}$  with a nominal value of  $361 \text{ K}$ .

11 gives a sense for the possible uncertainty in our climate calculations, it does not self-consistently simulate haze, relative humidity and clouds feedbacks. A more comprehensive model is required to resolve these nuances.

Moreover, our photochemical model does not include ion chemistry, which is likely a reasonable simplification because ions are not important for HCN or HCCCN formation on Titan (Loison et al. 2015). Only some heavy hydrocarbons, like benzene ( $\text{C}_6\text{H}_6$ ), rely on coupled neutral-ion chemistry to explain their observed abundances in Titan’s atmosphere (Hörst 2017).

## 5. CONCLUSIONS

We use atmospheric models to investigate the production of prebiotic feedstock molecules in impact-generated reducing atmospheres on the Hadean Earth, updating simpler calculations made by Zahnle et al. (2020). We find that massive asteroid impacts can generate temporary  $\text{H}_2$ -,  $\text{CH}_4$ - and  $\text{NH}_3$ -rich atmospheres, which photochemically generate HCN and HCCCN for the duration of hydrogen escape to space ( $10^5$  to  $10^7$  years). The production of nitriles increases dramatically for haze-rich atmospheres that have mole ratios of  $\text{CH}_4/\text{CO}_2 > 0.1$ . In these cases, HCN can rain out onto land surfaces at a rate of  $\sim 10^9 \text{ molecules cm}^{-2} \text{ s}^{-1}$ , and HCCCN incorporated in haze rains out at a similar rate. Atmospheres with  $\text{CH}_4/\text{CO}_2 < 0.1$  produce 3 to 4 orders of magnitude less HCN, and generate negligible HCCCN. The impactor mass required to create an atmosphere with  $\text{CH}_4/\text{CO}_2 > 0.1$  is uncertain and depends on

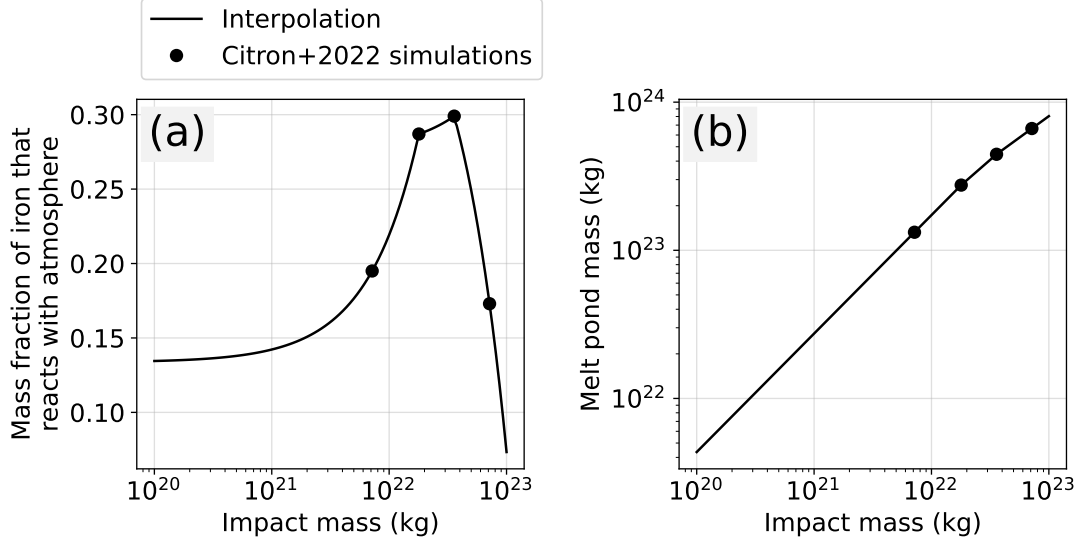


**Figure A1.** Interpolation and extrapolation of the Citron & Stewart (2022) SPH simulations of impacts that collide with Earth at a  $45^\circ$  angle and with a velocity of twice Earth’s escape velocity. (a) is the mass fraction of iron that reacts with the atmosphere and (b) is the mass of the melt pool produced by an impact. These interpolations are relevant to Figure 2 in the main text, and Appendix Figures A2, A3, A6, and A7.

how efficiently atmosphere-iron, atmosphere-melt and atmosphere-crust reactions generate  $H_2$  and the surface area of nickel catalysts exposed to the cooling steam atmosphere. In an optimistic modeling scenario a  $> 4 \times 10^{20}$  kg ( $> 570$  km) impactor is sufficient, while in our least optimistic scenario a  $> 5 \times 10^{21}$  kg ( $> 1330$  km) impactor is required.

We find that post-impact atmospheres that generate significant prebiotic molecules have  $> 360$  K surface temperatures caused by a  $H_2$ - $H_2$  greenhouse which may be too hot for prebiotic chemistry, although the temperature may be cooler if reflective clouds occur. An alternative is that HCN and HCCN generated in post-impact atmosphere are stockpiled. Cyanide can plausibly be stockpiled and concentrated in ferrocyanide salts and cyanoacetylene could be captured by byproducts of adenine synthesis into imidazole-based crystals (Ritson et al. 2022). HCN and HCCN can be used to create nucleotide precursors to RNA millions of years after the impact, once the  $H_2$  has escaped to space, and the atmosphere has cooled to a more temperate state.

Nominally, the Hadean Earth appears to have experienced several impacts that would have produced an atmosphere that made significant prebiotic feedstock molecules. Like Earth, all rocky exoplanets accreted from impacts. Consequently, impact-induced reducing atmospheres may be a common planetary processes that provides windows of opportunity for the origin of exoplanet life.

#### ACKNOWLEDGEMENTS

We thank Joshua Krissansen-Totton for numerous conversations that have improved the atmospheric models used in this article. Conversations with Maggie Thompson, Sandra Bastelberger, and Shawn Domagal-Goldman also helped us create the *Photochem* and *Clima* models. We also thank Eric Wolf for advice on computing reliable k-distributions for climate modeling. Additionally, we thank Paul Mollière for conversations that helped us build *Clima*. N.F.W. and D.C.C. were supported by the Simon’s Collaboration on Origin of Life Grant 511570 (to D.C.C.). Also, N.F.W., D.C.C., and K.J.Z. were supported by NASA Astrobiology Program Grant 80NSSC18K0829 and benefited from participation in the NASA Nexus for Exoplanet Systems Science research coordination network. N.F.W. and D.C.C. also acknowledge support from Sloan Foundation Grant G-2021-14194. R.L. and K.J.Z. were supported by NASA Exobiology Grant 80NSSC18K1082.

#### APPENDIX

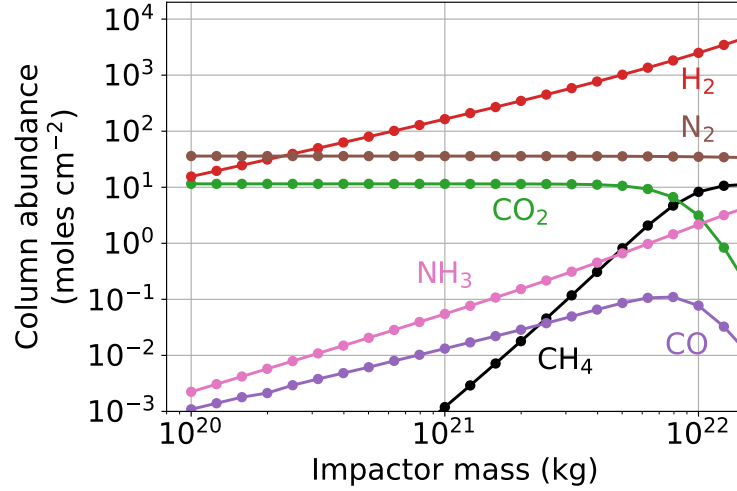


**Figure A2.** Identical to Figure 4 in the main text, but instead assumes post-impact  $H_2$  generation if governed by “Model 1B” described in Figure 2.

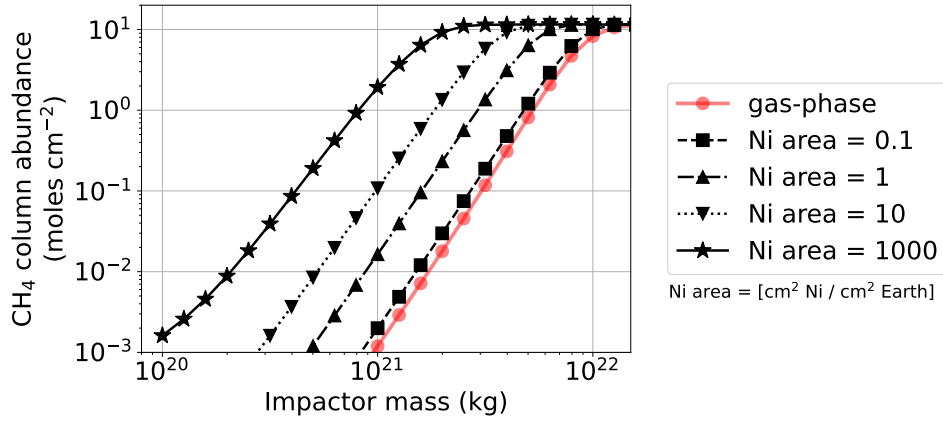


**Figure A3.** Identical to Figure 5 in the main text, but instead assumes post-impact  $H_2$  generation if governed by “Model 1B” described in Figure 2.

#### A. $H_2$ GENERATION FROM IRON AND MOLTEN CRUST

Here, we describe our model for atmospheric  $H_2$  generation in the days to months following a massive asteroid impact (Phase 1 in Figure 1). All our simulations assume a pre-impact atmosphere containing  $CO_2$ ,  $N_2$ , and ocean water. First, we assume that half of the impactor’s kinetic energy heats the atmosphere and ocean water to  $\sim 2000$  K. We assume the atmosphere is heated to  $\sim 2000$  K because this is roughly the evaporation temperature of silicates. For our assumed impact velocity of  $20.7 \text{ km s}^{-1}$ , all impactor masses that we consider in the main text ( $10^{20}$  to  $10^{22}$  kg) have kinetic energies  $> 2 \times 10^{28}$  joules delivering  $> 10^{28}$  joules to the atmosphere which is larger than the  $5 \times 10^{27}$  joules required to vaporize an ocean (Sleep et al. 1989).

Next, our model assumes each mole of iron delivered reacts with the atmosphere and removes one mole of oxygen. The moles  $\text{cm}^{-2}$  of iron delivered to the atmosphere is

$$N_{\text{Fe,atmos}} = \frac{X_{\text{Fe,atmos}} X_{\text{Fe,imp}} M_{\text{imp}}}{\mu_{\text{Fe}} A_{\oplus}} \quad (\text{A1})$$

Here,  $M_{\text{imp}}$  is the mass of the impact in grams,  $X_{\text{Fe,imp}}$  is the iron mass fraction of the impact,  $X_{\text{Fe,atmos}}$  is the fraction of the impactor iron that reacts with the atmosphere,  $\mu_{\text{Fe}}$  is the molar weight of iron, and  $A_{\oplus}$  is the area of Earth in  $\text{cm}^2$ . Following Zahnle et al. (2020) we take  $X_{\text{Fe,imp}} = 0.33$ . In main text, we assume  $X_{\text{Fe,atmos}} = 1$  (e.g. “Model 1A” in Figure 2), while the Appendix contains calculations with  $X_{\text{Fe,atmos}} = 0.15$  to  $0.3$  based on extrapolations of

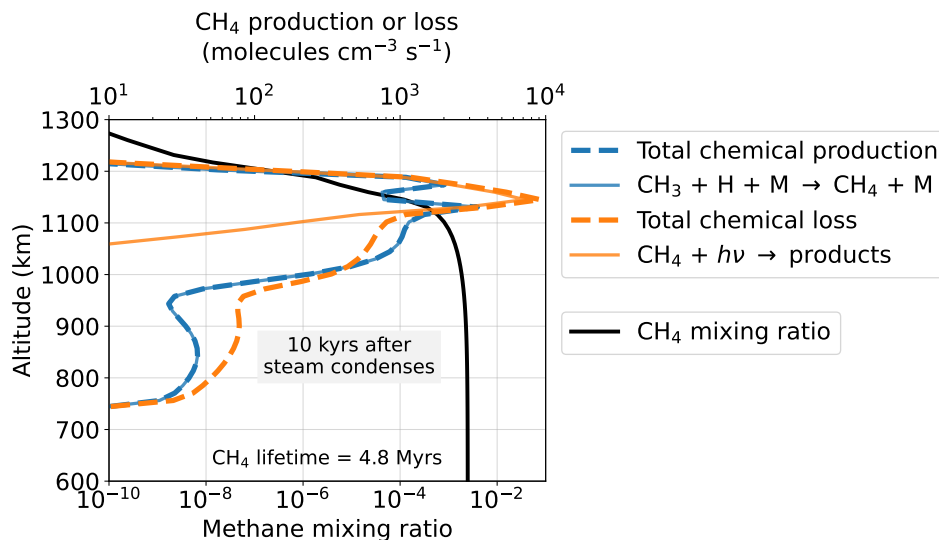


**Figure A4.** The methane photochemical lifetime in post-impact atmospheres. The plot shows the  $\text{CH}_4$  mixing ratio and production and loss as a function of altitude 10,000 years after the steam atmosphere has condensed to an ocean following the  $1.58 \times 10^{21}$  kg impact described in Figure 6.  $\text{CH}_4$  is primarily destroyed by photolysis, but reforms efficiently in the  $\text{H}_2$  rich atmosphere from  $\text{CH}_3 + \text{H} + \text{M} \rightarrow \text{CH}_4 + \text{M}$ . The result is a 4.8 million year  $\text{CH}_4$  photochemical lifetime.  $\text{CH}_4$  only persists in the atmosphere for about one million years because  $\text{H}_2$  escapes to space in this amount of time which inhibits  $\text{CH}_4$  recombination.

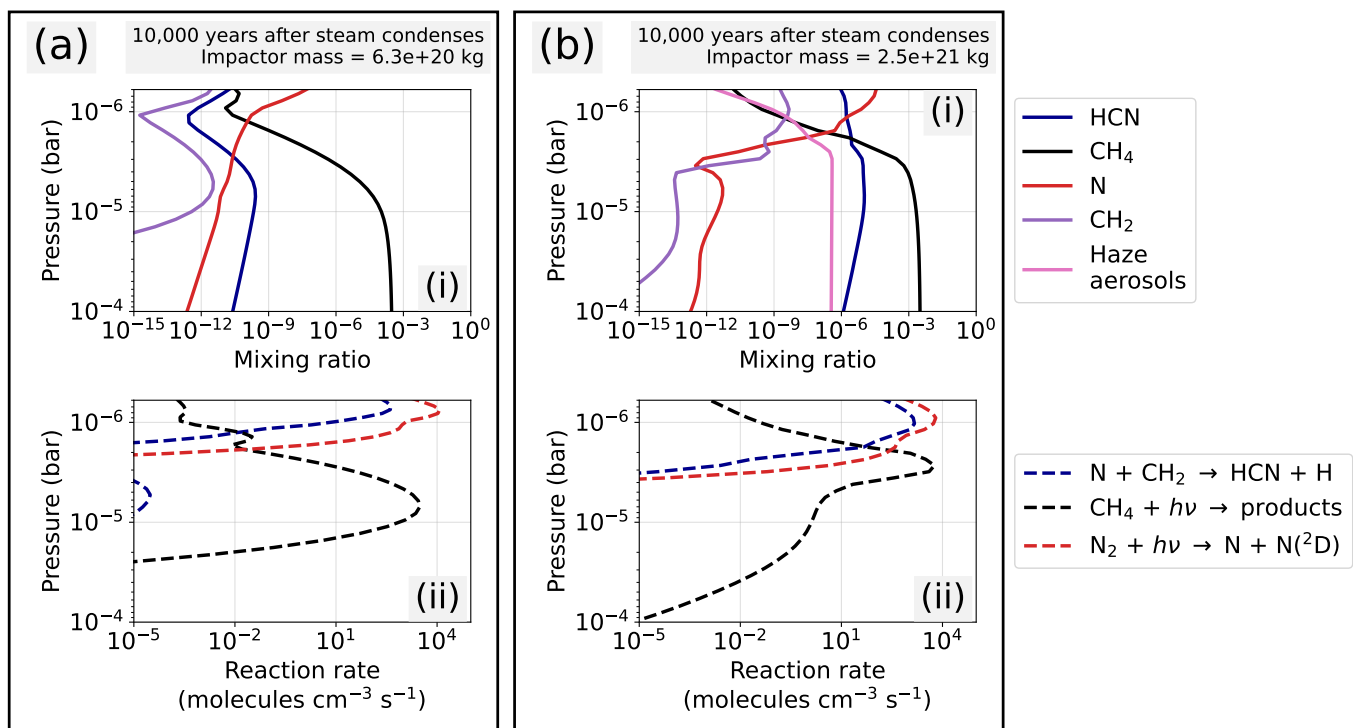


**Figure A5.** HCN production and precursor species after a (a)  $6.3 \times 10^{20}$  kg and (b)  $2.5 \times 10^{21}$  kg impactor. In both (a) and (b) panels (i) shows mixing ratios, while (ii) shows photolysis and reaction rates. Panel (b) contains haze aerosols which cause  $\text{CH}_4$  photolysis to be higher in the atmosphere compared to panel (a). High altitude  $\text{CH}_4$  photolysis, closer to  $\text{N}_2$  photolysis, promotes HCN production because photolysis produced can more readily combine to make cyanides.

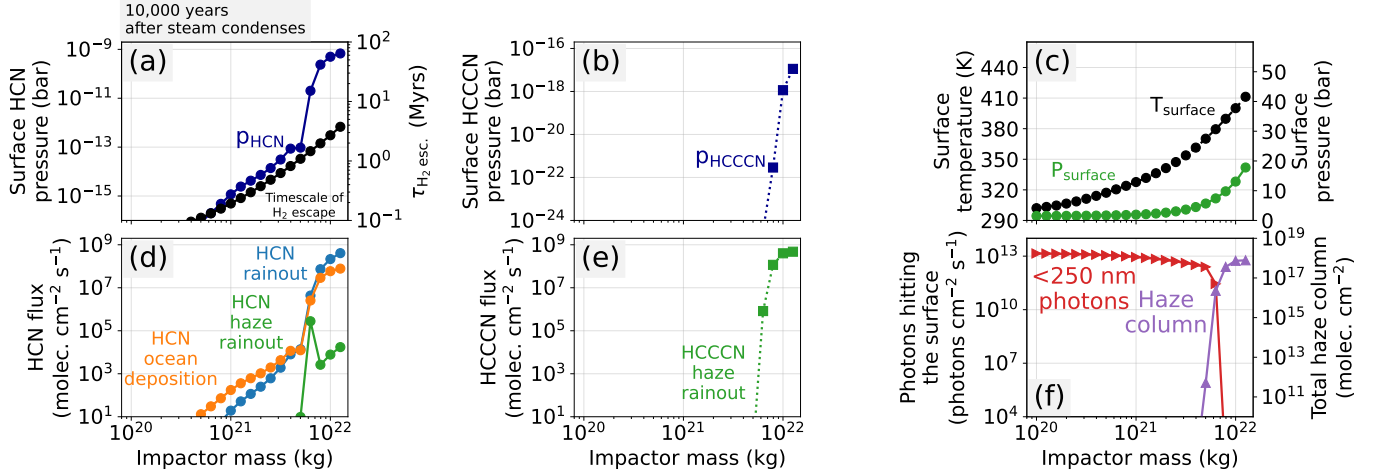


**Figure A6.** Identical to Figure 7 in the main text, but instead assumes post-impact  $H_2$  generation if governed by “Model 1B” described in Figure 2.

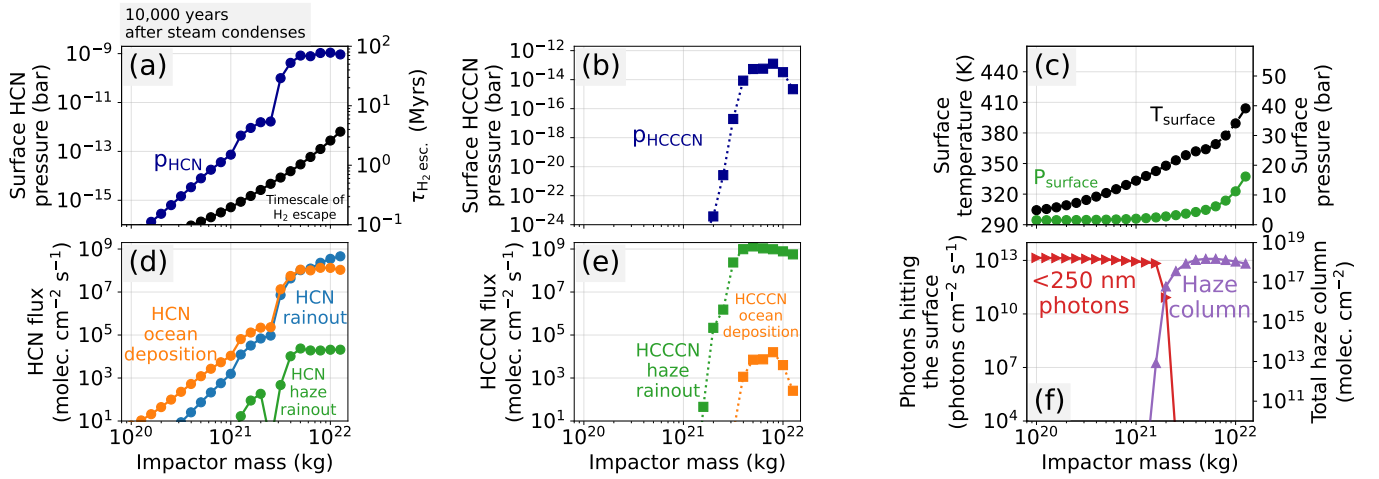


**Figure A7.** Identical to Figure 9 in the main text, but instead assumes post-impact  $H_2$  generation if governed by “Model 1B” described in Figure 2.

the Citron & Stewart (2022) SPH impact simulations for  $45^\circ$  impactors traveling at  $20.7 \text{ km s}^{-1}$  (e.g. “Model 1B” in Figure 2). To approximate equilibration between the delivered iron and the atmosphere, we simply remove  $N_{\text{Fe,atmos}}$  of O from the atmosphere.

Our model also optionally considers reactions between the atmosphere and a melt pond generated by the impact. Our approach is similar to the one described in Itcovitz et al. (2022). We estimate the total mass of the melt pond ( $M_{\text{melt}}$ ) by interpolating SPH impact simulations from Citron & Stewart (2022) for a  $45^\circ$  impact angle. The smallest impact they consider is  $7 \times 10^{21} \text{ kg}$ , so we extrapolate their results down to  $10^{20} \text{ kg}$ . We additionally take the melted crust to be basaltic in composition except with variable initial amounts of ferric and ferrous iron. Effectively, this means that the initial oxygen fugacity of the melted crust is a free parameter because iron redox state is related to oxygen fugacity through the equilibrium reaction,



We assume the oxygen atoms can flow from the atmosphere into the melt (or vice-versa) in order to bring Reaction A2 to an equilibrium state defined by Kress & Carmichael (1991) thermodynamic data. Our model also considers  $H_2O$  gas dissolution in the melt using the Equation (19) solubility relation in Itcovitz et al. (2022).



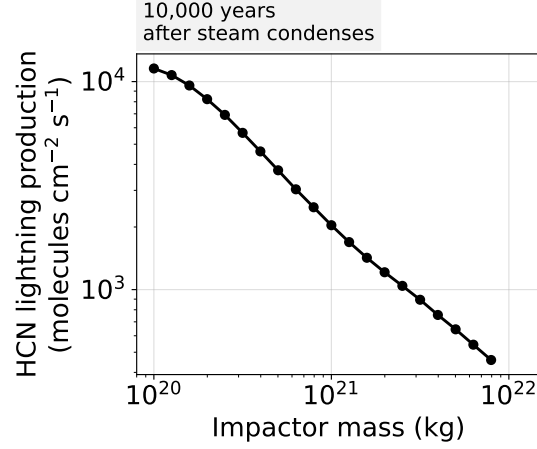


**Figure A8.** HCN production from lightning for the same simulations and time-period shown in Figure 7. The calculations use methods described in Chameides & Walker (1981) assuming modern Earth’s lightning dissipation rate ( $9.8 \times 10^{-9} \text{ J cm}^{-2} \text{ s}^{-1}$ ), and a 2250 K HCN freeze-out temperature. HCN production from lightning is small compared to what is achievable with photochemistry.

Finally, given a heated post-impact atmosphere that has been reduced by impactor iron and, optionally, in contact with an melt pool, we compute thermodynamic equilibrium of the atmosphere-melt system at 1900 K. We choose 1900 K because any impact-produced silicate vapors should have condensed and rained out of the atmosphere, and the melt pool should have not yet solidified (Itcovitz et al. 2022). To find an equilibrium state, we first compute an equilibrium composition for the atmosphere alone using the equilibrium solver in the Cantera chemical engineering package (Goodwin et al. 2022) with our thermodynamic data (Appendix C.2). Next, to equilibrate the atmosphere-melt system, we perform a zero-dimensional kinetics integration for 1000 years at constant temperature and pressure with our reaction network (Appendix C.2). All reactions in our network are reversible thermodynamically, therefore integrating the kinetics forward in time should ultimately reach a state of thermodynamic equilibrium. Our integration includes additional reactions representing Reaction A2 and H<sub>2</sub>O dissolution in the melt. We arbitrarily choose forward reaction rates of  $10^{-10} \text{ s}^{-1}$  for both reactions, then reverse the rates using the Kress & Carmichael (1991) equilibrium constant, and the Equation (19) solubility relation in Itcovitz et al. (2022). Overall, our approach finds a chemical equilibrium state between the atmosphere and the melt pond, and therefore an estimation of the amount of H<sub>2</sub> generated from atmosphere-iron and atmosphere-melt reactions.

Our code for solving melt-atmosphere equilibrium is available at the following Zenodo link: <https://doi.org/10.5281/zenodo.7802966>.

## B. KINETICS MODEL OF A COOLING STEAM ATMOSPHERE

We simulate the chemistry of a cooling post-impact atmosphere using a zero-dimensional kinetics-climate model. We assume the atmosphere’s composition, pressure, and temperature are homogeneous in all directions, and has a vertical extent of one atmospheric scale height ( $H_a$ ). For these assumptions, the following system of ordinary differential equations govern our model:

$$\frac{\partial N_i}{\partial t} = \frac{H_a}{N_a}(P_i - L_i) + \frac{A_c}{N_a}(P_{i,\text{surf}} - L_{i,\text{surf}}) \quad (\text{B3})$$

$$\frac{\partial T_s}{\partial t} = -\frac{1}{\rho c_p} \left( \frac{F_{\text{net}}}{H_a} \right) - \frac{1}{\rho c_p} \left( \frac{dM_{\text{H}_2\text{O}}}{dt} \frac{l_{\text{H}_2\text{O}}}{A_{\oplus} H_a} \right) \quad (\text{B4})$$

All variables and units are in Table A1. In Equation (B3),  $N_i$  is the column abundance of species  $i$  in mole  $\text{cm}^{-2}$ , which changes because of gas-phase chemical reactions (production rate  $P_i$  and loss rate  $L_i$ ) and reactions occurring on surfaces ( $P_{i,\text{surf}}$  and  $L_{i,\text{surf}}$ ). In Equation (B4),  $T$  is surface temperature, which changes because of energy radiated to space ( $F_{\text{net}}$ ), and because of latent heat from H<sub>2</sub>O condensation ( $\frac{dM_{\text{H}_2\text{O}}}{dt}$ ), where  $M_{\text{H}_2\text{O}}$  is the mass of H<sub>2</sub>O in the atmosphere. We approximate the energy radiated to space in  $\text{ergs cm}^{-2} \text{ s}^{-1}$  from a steam-dominated atmosphere with the following parameterization:

$$F_{\text{net}} = 8.3 \times 10^4 + 1000 \max(T_s - 1750, 0) \quad (\text{B5})$$

This parameterization fits calculations from our radiative transfer model (see Appendix D), which uses the a solar spectrum at 4.0 Ga derived from methods described in [Claire et al. \(2012\)](#).

We can rewrite Equation (B4), replacing  $\rho H_a$  using the ideal gas law and the definition of atmospheric scale height,

$$\rho H_a = \frac{p\bar{\mu}}{N_a k T} \frac{N_a k T}{\bar{\mu} g} = \frac{p}{g} \quad (\text{B6})$$

Here,  $p$  is the total atmospheric pressure in dynes  $\text{cm}^{-2}$ ,  $g$  is gravitational acceleration in  $\text{cm s}^{-2}$ ,  $k$  is the Boltzmann constant,  $\bar{\mu}$  is the mean molecular weight in  $\text{g mol}^{-1}$ , and  $N_a$  is Avogadro's number. Therefore,

$$\frac{\partial T_s}{\partial t} = -\frac{g}{p c_p} F_{\text{net}} - \frac{g}{p c_p} \left( \frac{dM_{\text{H}_2\text{O}}}{dt} \frac{l_{\text{H}_2\text{O}}}{A_{\oplus}} \right) \quad (\text{B7})$$

Next, we must derive an expression for the steam condensation rate ( $dM_{\text{H}_2\text{O}}/dt$ ) in terms of known variables. Working in CGS units, the total pressure of the atmosphere is given by its gravitational force divided by Earth's surface area ( $5.1 \times 10^{18} \text{ cm}^2$ ):

$$p = \frac{Mg}{A_{\oplus}} \quad (\text{B8})$$

Here,  $M$  is the mass of the atmosphere in grams. We are considering steam-dominated atmospheres, therefore, the mass and pressure in the above relation is approximately equal to the mass of atmospheric  $\text{H}_2\text{O}$  and the  $\text{H}_2\text{O}$  partial pressure.

$$p_{\text{H}_2\text{O}} \approx \frac{M_{\text{H}_2\text{O}} g}{A_{\oplus}} \quad (\text{B9})$$

$$M_{\text{H}_2\text{O}} \approx \frac{p_{\text{H}_2\text{O}} A_{\oplus}}{g} \quad (\text{B10})$$

Taking a time derivative of Equation (B10) yields

$$\frac{dM_{\text{H}_2\text{O}}}{dt} \approx \frac{A_{\oplus}}{g} \frac{dp_{\text{H}_2\text{O}}}{dt} \quad (\text{B11})$$

We assume that the only processes changing the  $\text{H}_2\text{O}$  mass in the atmosphere is condensation, which occurs in our model when steam becomes saturated. We further assume that the  $\text{H}_2\text{O}$  partial pressure is fixed at saturation once steam condensation begins. We approximate the saturation vapor pressure of  $\text{H}_2\text{O}$ ,  $p_{\text{H}_2\text{O}}^{\text{sat}}$ , using the Clausius-Clapeyron equation, assuming a temperature-independent latent heat,  $l_{\text{H}_2\text{O}}$ ,

$$p_{\text{H}_2\text{O}}^{\text{sat}} = p_0 \exp \left( \frac{l_{\text{H}_2\text{O}} \mu_{\text{H}_2\text{O}}}{R} \left( \frac{1}{T_0} - \frac{1}{T} \right) \right) \quad (\text{B12})$$

$p_0$  and  $T_0$  are reference pressures and temperatures, respectively. Taking a time derivative of Equation (B12) yields

$$\frac{dp_{\text{H}_2\text{O}}^{\text{sat}}}{dt} = \left( \frac{l_{\text{H}_2\text{O}} \mu_{\text{H}_2\text{O}}}{RT^2} \right) \frac{dT_s}{dt} p_{\text{H}_2\text{O}}^{\text{sat}} \quad (\text{B13})$$

Substituting Equation (B13) into Equation (B11) gives

$$\frac{dM_{\text{H}_2\text{O}}}{dt} = \frac{A_{\oplus}}{g} \left( \frac{l_{\text{H}_2\text{O}} \mu_{\text{H}_2\text{O}}}{RT^2} \right) \frac{dT_s}{dt} p_{\text{H}_2\text{O}}^{\text{sat}} \quad (\text{B14})$$

Finally, we can substitute Equation (B14) into Equation (B7) and rearrange to solve for  $dT/dt$ . The result below gives the rate of change of temperature when the steam is too hot to condense ( $p_{\text{H}_2\text{O}} > p_{\text{H}_2\text{O}}^{\text{sat}}$ ), and when the steam is

condensing ( $p_{\text{H}_2\text{O}} = p_{\text{H}_2\text{O}}^{\text{sat}}$ ).

$$\frac{dT_s}{dt} = \begin{cases} -\frac{g}{pc_p} F_{\text{net}} & p_{\text{H}_2\text{O}} > p_{\text{H}_2\text{O}}^{\text{sat}} \\ -\frac{g}{pc_p} F_{\text{net}} \left( 1 + \frac{l_{\text{H}_2\text{O}}^2 \mu_{\text{H}_2\text{O}} p_{\text{H}_2\text{O}}^{\text{sat}}}{pc_p RT^2} \right)^{-1} & p_{\text{H}_2\text{O}} = p_{\text{H}_2\text{O}}^{\text{sat}} \end{cases} \quad (\text{B15})$$

Equations (B3) and (B15) are a system of ordinary differential equations, which we approximately solve over time using the CVODE BDF method developed by Sundials Computing (Hindmarsh et al. 2005). Additionally, for either gas-phase or surface reactions, we make use of the Cantera software library (Goodwin et al. 2022) to compute chemical production and destruction rates. Our code for solving the equations derived in this section is available at the following Zenodo link: <https://doi.org/10.5281/zenodo.7802966>.

### C. THE *PHOTOCHEM* MODEL

To simulate the photochemistry of post-impact reducing atmospheres, we developed a photochemical model called *Photochem*. The model is a re-written and vastly updated version of *PhotochemPy* (Wogan et al. 2022). *Photochem* is written in modern Fortran and C, with a Python interface made possible by Cython (Behnel et al. 2010). This article uses *Photochem* version v0.3.14 archived in the following Zenodo repository: <https://doi.org/10.5281/zenodo.7802921>.

The following sections briefly describe the fundamental model equations solved by *Photochem*, our chemical network, and validates the model against observations of Earth and Titan.

#### C.1. Model equations

We begin our derivation of the equations governing *Photochem* with modified versions of Equations B.1, B.2 and B.29 in Catling & Kasting (2017):

$$\frac{\partial n_i}{\partial t} = -\frac{\partial}{\partial z} \Phi_i + P_i - L_i - R_{i, \text{rainout}} + Q_{i, \text{cond}} \quad (\text{C16})$$

$$\Phi_{i, \text{gas}} = -K_{zz} n \frac{\partial}{\partial z} \left( \frac{n_i}{n} \right) - n_i D_i \left( \frac{1}{n_i} \frac{\partial n_i}{\partial z} + \frac{1}{H_i} + \frac{1}{T} \frac{\partial T}{\partial z} + \frac{\alpha_{Ti}}{T} \frac{\partial T}{\partial z} \right) \quad (\text{C17})$$

$$\Phi_{i, \text{particle}} = -K_{zz} n \frac{\partial}{\partial z} \left( \frac{n_i}{n} \right) - w_i n_i \quad (\text{C18})$$

Table A1 explains the variables and their units. Equation (C16) states that molecule concentration ( $n_i$  in molecules  $\text{cm}^{-3}$ ) changes over time at a point in space because of vertical movement of particles ( $\frac{\partial}{\partial z} \Phi_i$ ), and chemical reactions, rainout or condensation/evaporation ( $P_i$ ,  $L_i$ ,  $R_{i, \text{rainout}}$ , and  $Q_{i, \text{cond}}$ ). The equation is 1-D, because it only considers vertical gas transport and differs from Equation B.1 in Catling & Kasting (2017) because we explicitly include rainout and condensation. Equation (C17) states that the flux of gases ( $\Phi_{i, \text{gas}}$ ) is determined by eddy and molecular diffusion, and Equation (C18) assumes that the flux of particles ( $\Phi_{i, \text{particle}}$ ) is given by eddy diffusion and the rate particles fall through the atmosphere.

Many 1-D photochemical models further simplify Equation (C16) by assuming that total number density does not change over time ( $\partial n / \partial t \approx 0$ ). Using this assumption, Equation (C16) is recast in terms of evolving mixing ratios ( $f_i$ ) rather than number densities (see Appendix B.1 in Catling & Kasting (2017) for a derivation). Such models assume a time-constant temperature profile. The surface pressure is also prescribed, and pressures above the surface are computed with the hydrostatic equation. In order to guarantee that all mixing ratios in the atmosphere sum to 1, models assume a background filler gas with a mixing ratio  $f_{\text{background}} = 1 - \sum_i f_i$ .  $\text{N}_2$ ,  $\text{CO}_2$  or  $\text{H}_2$  are common choices for the background gas, depending on the atmosphere under investigation. By definition, the background gas is not conserved. This approach is valid for steady-state photochemical calculations, and is also reasonable for atmospheric transitions which maintain approximately constant surface pressure and atmospheric temperature. The *Photochem* code contains an implementation of this traditional approach to photochemical modeling.

Unfortunately, solving a simplified version of Equation (C16) in terms of mixing ratios does not work well for post-impact atmospheric modeling. For example, a post-impact atmosphere can contain 10 bars of  $\text{H}_2$  which escapes to space over millions of years, lowering the surface pressure to a 1 bar  $\text{N}_2$  dominated atmosphere (e.g. Figure 6). Traditional photochemical models fail to simulate this scenario because it is not reasonable to assume a single background gas

**Table A1.** Variables

Variable	Definition	Units
$f_i$	Mixing ratio of species $i$	dimensionless
$n_i$	Number density of species $i$	molecules $\text{cm}^{-3}$
$n$	Total number density	molecules $\text{cm}^{-3}$
$N_i$	Column abundance of species $i$	$\text{mol cm}^{-2}$
$N$	Total column abundance	$\text{mol cm}^{-2}$
$\rho$	Density of the atmosphere	$\text{g cm}^{-3}$
$c_p$	Specific heat capacity of the atmosphere	$\text{erg g}^{-1} \text{K}^{-1}$
$F_{\text{net}}$	Net radiative energy leaving the atmosphere	$\text{erg cm}^{-2} \text{s}^{-1}$
$z$	Altitude	cm
$t$	Time	seconds
$P_i$	Total chemical production of species $i$	molecules $\text{cm}^{-3} \text{s}^{-1}$
$L_i$	Total chemical loss of species $i$	molecules $\text{cm}^{-3} \text{s}^{-1}$
$P_{i,\text{surf}}$	Total chemical production of species $i$ from surface reactions	molecules $\text{cm}^{-2} \text{s}^{-1}$
$L_{i,\text{surf}}$	Total chemical loss of species $i$ from surface reactions	molecules $\text{cm}^{-2} \text{s}^{-1}$
$R_{i,\text{rainout}}$	Production and loss of species $i$ from rainout	molecules $\text{cm}^{-3} \text{s}^{-1}$
$Q_{i,\text{cond}}$	Production and loss of species $i$ from condensation and evaporation	molecules $\text{cm}^{-3} \text{s}^{-1}$
$\Phi_i$	Vertical flux of species $i$	molecules $\text{cm}^{-2} \text{s}^{-1}$
$K_{zz}$	Eddy diffusion coefficient	$\text{cm}^{-2} \text{s}^{-1}$
$D_i$	Molecular diffusion coefficient	$\text{cm}^{-2} \text{s}^{-1}$
$H_i$	$= N_a k T / \mu_i g$ , The scale heights of species $i$	cm
$H_a$	$= N_a k T / \bar{\mu} g$ , The average scale height.	cm
$N_a$	Avogadro's number	molecules $\text{mol}^{-1}$
$k$	Boltzmann's constant	$\text{erg K}^{-1}$
$R$	Gas constant	$\text{erg mol}^{-1} \text{K}^{-1}$
$\mu$	Molar mass. $\bar{\mu}$ is mean molar mass of the atmosphere, and $\mu_i$ is the molar mass of species $i$	$\text{g mol}^{-1}$
$A_c$	Catalyst surface area per atmospheric column	$\text{cm}^2 \text{catalyst} / \text{cm}^2 \text{Earth}$
$l_{\text{H}_2\text{O}}$	Latent heat of $\text{H}_2\text{O}$ condensation	$\text{erg g}^{-1}$
$A_{\oplus}$	Area of Earth's surface	$\text{cm}^2$
$\phi$	Relative humidity	dimensionless
$A_s$	Optical surface albedo	dimensionless
$p$	Atmospheric pressure. $p_i$ is the partial pressure of species $i$ .	$\text{dynes cm}^{-2}$
$M$	Mass of the atmosphere. $M_i$ is the mass of species $i$ . $M_{\text{imp}}$ is the mass of an impactor.	g
$g$	Gravitational acceleration	$\text{cm s}^{-2}$
$\alpha_{\text{Ti}}$	Thermal diffusion coefficient of species $i$ . We neglect this term ( $\alpha_{\text{Ti}} = 0$ )	dimensionless
$T$	Temperature. $T_s$ is the surface temperature.	K

and time-constant surface pressure. Additionally, most models fix atmospheric temperature during any single model integration, but surface temperature should change significantly as impact-generated  $\text{H}_2$  escapes to space.

Therefore, *Photochem* implements a code that solves Equation (C16) in terms of number densities ( $n_i$ ) without the assumption of fixed surface pressure or a background gas. This approach requires slight modifications to Equation (C17) and (C18) which we describe below. Consider the hydrostatic equation and ideal gas law

$$\frac{\partial p}{\partial z} = \frac{-gp\bar{\mu}}{N_a k T} \quad (\text{C19})$$

$$p = nkT \quad (\text{C20})$$

Substituting the ideal gas law in the hydrostatic equation yields

$$\frac{\partial}{\partial z}(nT) = \frac{-gn\bar{\mu}}{N_a k} \quad (\text{C21})$$

$$n \frac{\partial T}{\partial z} + T \frac{\partial n}{\partial z} = \frac{-gn\bar{\mu}}{N_a k} \quad (\text{C22})$$

After rearrangement and substituting the definition of scale height,

$$\frac{1}{n} \frac{\partial n}{\partial z} = -\frac{1}{H_a} - \frac{1}{T} \frac{\partial T}{\partial z} \quad (\text{C23})$$

Now consider the following expansion using the quotient rule

$$\frac{\partial}{\partial z} \left( \frac{n_i}{n} \right) = \frac{1}{n} \frac{\partial n_i}{\partial z} - \frac{n_i}{n^2} \frac{\partial n}{\partial z} \quad (\text{C24})$$

Substituting Equation (C23) into Equation (C24) and rearrangement gives

$$n \frac{\partial}{\partial z} \left( \frac{n_i}{n} \right) = \frac{\partial n_i}{\partial z} + \frac{n_i}{H_a} + \frac{n_i}{T} \frac{\partial T}{\partial z} \quad (\text{C25})$$

Finally, we can substitute Equation (C25) into Equations (C17) and (C18) to derive new equations for the flux of gases and particles

$$\Phi_{i,\text{gas}} = -K_{zz} n_i \left( \frac{1}{n_i} \frac{\partial n_i}{\partial z} + \frac{1}{H_a} + \frac{1}{T} \frac{\partial T}{\partial z} \right) - n_i D_i \left( \frac{1}{n_i} \frac{\partial n_i}{\partial z} + \frac{1}{H_i} + \frac{1}{T} \frac{\partial T}{\partial z} + \frac{\alpha_{Ti}}{T} \frac{\partial T}{\partial z} \right) \quad (\text{C26})$$

$$\Phi_{i,\text{particle}} = -K_{zz} n_i \left( \frac{1}{n_i} \frac{\partial n_i}{\partial z} + \frac{1}{H_a} + \frac{1}{T} \frac{\partial T}{\partial z} \right) - w_i n_i \quad (\text{C27})$$

We then apply a finite-volume approximation to the Equation (C16) system of particle differential equations using fluxes for gases and particles given by Equations (C26) and (C27), which results in a system of ordinary differential equations. We use a second-order centered scheme for all spatial derivatives except falling particles, which use a first-order upwind scheme for stability. *Photochem* evolves the finite volume approximate forward in time using the CVODE BDF method developed by Sundials Computing (Hindmarsh et al. 2005). The model assumes no background gas, and surface pressure can evolve over time as, for example, gases escape to space. Additionally, our model computes a self-consistent temperature structure within each time step using the *Clima* radiative transfer code (Appendix D) assuming a pseudo-moist adiabat troposphere connected to an isothermal upper atmosphere.

An additional challenge of post-impact atmospheres is that the scale height changes by a factor of  $\sim 10$  or more when  $\text{H}_2$  escapes leaving behind a  $\text{N}_2$  or  $\text{CO}_2$  dominated atmosphere (Figure 6). Most relevant photochemistry occurs at pressures  $> 10^{-7}$  bar, and so we choose a model domain which starts at the surface and extends to an altitude that is approximately this pressure. However, suppose we choose a model domain extending to  $\sim 1000$  km (i.e. the  $10^{-7}$  bar level) appropriate for an  $\text{H}_2$  dominated atmosphere. After  $\text{H}_2$  escapes to space, all relevant photochemistry would occur below 100 km, in the bottom several grid cells of the model. Therefore, the important photochemistry would be poorly resolved and inaccurate, and the extremely small pressures at the top of the model domain would likely cause numerical instability. Our solution is to adaptively adjust the model domain so it is always appropriate for atmospheres scale height. We use the root finding functionality in CVODE BDF to halt integration whenever the pressure at the top of the atmosphere falls below  $10^{-7}$  bar and lower the top of the model domain before continuing integration. This procedure is done automatically tens to hundreds of times during each post-impact integration.

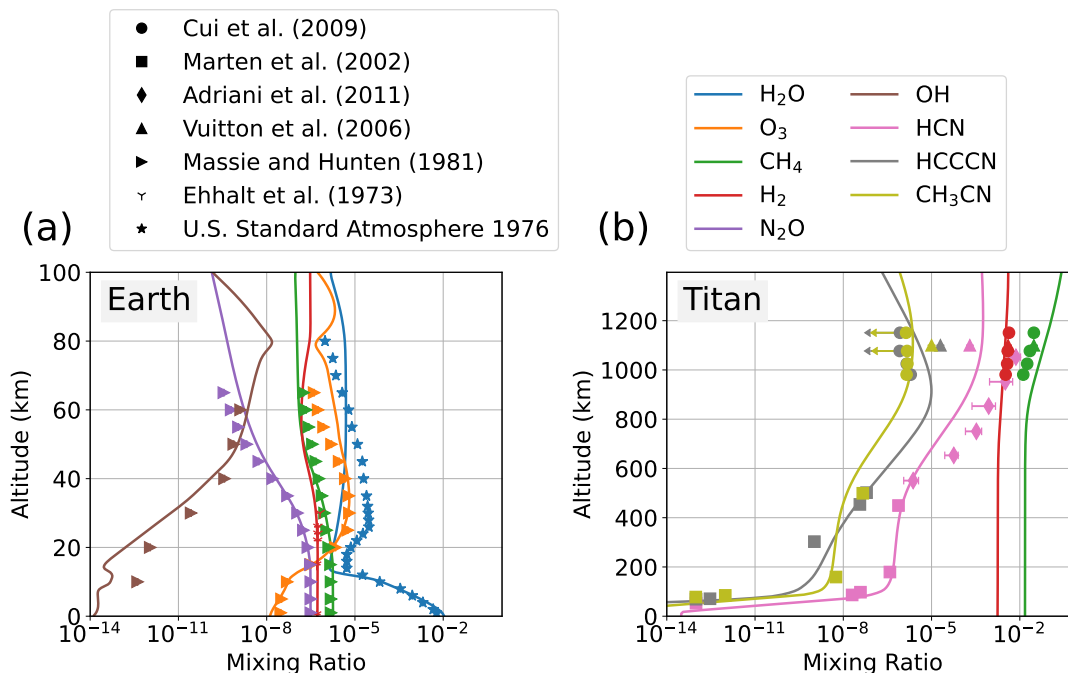


**Figure A9.** Earth and Titan photochemical model validation. (a) and (b) shows the *Photochem* model applied to Earth and Titan, respectively, compared to data from the literature (Cui et al. 2009; Marten et al. 2002; Adriani et al. 2011; Vuitton et al. 2006; Massie & Hunten 1981; Ehhalt et al. 1975).

## C.2. Chemical network, photolysis cross sections and thermodynamic data

Our chemical reactions, photolysis cross sections, and thermodynamic data used for all gas-phase kinetics are archived in the following Zenodo repository: <https://doi.org/10.5281/zenodo.7802962>. Chemical reactions and thermodynamic data are in the file “reaction\_mechanisms/zahnle-earth.yaml”, and photolysis cross sections are in the folder “xsections/”. All thermodynamic data is from the NIST Chemistry WebBook. The chemical and photolysis reactions are an updated version of rates presented in Zahnle et al. (2016).

## C.3. Model validation

Figure A9 shows *Photochem* applied to Earth and Titan compared to observations gathered from the literature. All boundary conditions and settings for each model are archived in the “ModernEarth” and “Titan” templates in the following Zenodo repository: <https://doi.org/10.5281/zenodo.7802921>. Our model of Titan fixes the surface CH<sub>4</sub> mixing ratio to 0.015 volume mixing ratio, permits H<sub>2</sub> escape at the diffusion-limited rate, and allows aerosols to fall to Titan’s surface, but otherwise has zero-flux boundary conditions. We ignore the effects of galactic cosmic rays, which causes our model to under-predict the nitrile production in the lower atmosphere (Lavvas et al. 2008b). Additionally, we neglect ion chemistry which is argued to be important for the formation of large hydrocarbons (e.g., C<sub>6</sub>H<sub>6</sub>), but inconsequential for smaller molecular weight species. Despite these omissions, *Photochem* broadly reproduces the main cyanide chemistry on Titan.

## C.4. Deposition velocity of HCN

Our photochemical-climate simulations of post-impact atmosphere assume a HCN surface deposition velocity of  $7 \times 10^{-3} \text{ cm s}^{-1}$ . Here, we describe a simple model of HCN hydrolysis in the ocean which justifies this value.

Motivated by Appendix 3 in Kharecha et al. (2005), we imagine a two-box ocean model with a surface ocean of depth  $\sim 100 \text{ m}$  and a deep ocean ( $\sim 4 \text{ km}$ ). We assume HCN transport into the ocean is governed by a stagnant boundary layer model (see Figure 3 in Kharecha et al. (2005)), where it is destroyed by hydrolysis reactions. HCN is mixed between the surface and deep ocean reservoirs by a turnover velocity,  $v_{\text{over}}$ , which we nominally take to be  $1.2 \times 10^{-5} \text{ cm s}^{-1}$  which is appropriate for modern Earth. Under these circumstances, the following system of ordinary differential equations governs the concentration of HCN in the surface and deep ocean.



$$\frac{dm_{\text{HCN},s}}{dt} = \frac{\Phi_{\text{HCN}}}{Cz_s} - k_{\text{tot}}m_{\text{HCN},s} - \left(\frac{v_{\text{over}}}{z_s}\right)(m_{\text{HCN},s} - m_{\text{HCN},d}) \quad (\text{C28})$$

$$\frac{dm_{\text{HCN},d}}{dt} = -k_{\text{tot}}m_{\text{HCN},s} + \left(\frac{v_{\text{over}}}{z_d}\right)(m_{\text{HCN},s} - m_{\text{HCN},d}) \quad (\text{C29})$$

Here,  $m_{\text{HCN},s}$  and  $m_{\text{HCN},d}$  are the concentration of HCN in the surface and deep ocean, respectively, in  $\text{mol L}^{-1}$ ,  $C$  is a constant equal to  $6.022 \times 10^{20} \text{ molecules mol}^{-1} \text{ L cm}^{-3}$ ,  $z_s$  is the depth of the surface ocean, and  $z_d$  is the depth of the deep ocean. We compute the temperature and pH dependent hydrolysis rate coefficient,  $k_{\text{tot}}$ , following Miyakawa et al. (2002).  $\Phi_{\text{HCN}}$  is the HCN flux into the ocean in  $\text{molecules cm}^{-2} \text{ s}^{-1}$ , which is determined by a stagnant boundary layer model:

$$\Phi_{\text{HCN}} = v_{\text{p,HCN}}(\alpha_{\text{HCN}}10^{-6}p_{\text{HCN}} - m_{\text{HCN},s})C \quad (\text{C30})$$

We assume the piston velocity of HCN is  $5 \times 10^{-3} \text{ cm s}^{-1}$ , which is the same as the piston velocity of CO (Kharecha et al. 2005, Table 1). Also,  $\alpha_{\text{HCN}}$  is the Henry's law coefficient for HCN. The flux of a gas can also be parameterized with a deposition velocity ( $v_{\text{d,HCN}}$ ):

$$\begin{aligned} \Phi_{\text{HCN}} &= n_{\text{HCN}}v_{\text{d,HCN}} \\ &= \frac{p_{\text{HCN}}}{kT}v_{\text{d,HCN}} \end{aligned} \quad (\text{C31})$$

Assuming a steady state ( $dm_{\text{HCN},s}/dt = dm_{\text{HCN},d}/dt = 0$ ) and solving for  $v_{\text{d,HCN}}$  in Equations (C28) - (C31) yields

$$v_{\text{d,HCN}} = 10^{-6}kT\alpha_{\text{HCN}}Ck_{\text{tot}}v_{\text{p,HCN}} \frac{k_{\text{tot}}z_dz_s + v_{\text{over}}(z_d + z_s)}{k_{\text{tot}}z_d(v_{\text{p,HCN}} + k_{\text{tot}}z_s) + v_{\text{over}}(v_{\text{p,HCN}} + k_{\text{tot}}(z_d + z_s))} \quad (\text{C32})$$

Here, we assume that the temperature and pH of the ocean is uniform, and that the temperature of the surface air is the same as the temperature of the ocean.

Figure A10 computes the deposition velocity of HCN using Equation (C32) over a wide range of ocean temperatures and pH. Kadoya et al. (2020) used a model of the geologic carbon cycle to argue that the Hadean ocean was moderately alkaline ( $\text{pH} \approx 8$ ). Therefore, we choose a HCN deposition velocity of  $7 \times 10^{-3} \text{ cm s}^{-1}$  for our nominal model because it is a reasonable approximation of the  $\text{pH} = 8$  case over a wide range of temperatures. Additionally, we assume that HCCCN has the same deposition velocity as HCN, also caused by hydrolysis reactions in the ocean.

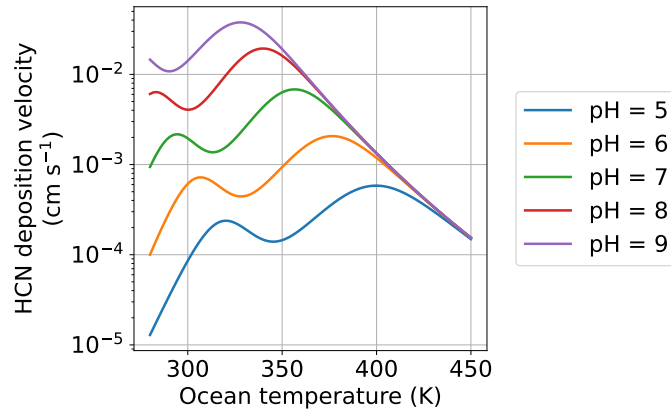
We have re-run our photochemical-climate simulations of post-impact atmospheres with order-of-magnitude larger and smaller HCN deposition velocities. The results are qualitatively unchanged. For example, assuming  $v_{\text{d,HCN}} = 7 \times 10^{-4} \text{ cm s}^{-1}$  for a  $2 \times 10^{21} \text{ kg}$  impactor in Figure 7 causes one order of magnitude smaller HCN ocean deposition. However, the HCN rainout and HCN surface pressure is unchanged because HCN rainout dominates over the HCN ocean deposition.

#### D. THE CLIMA RADIATIVE TRANSFER AND CLIMATE MODEL

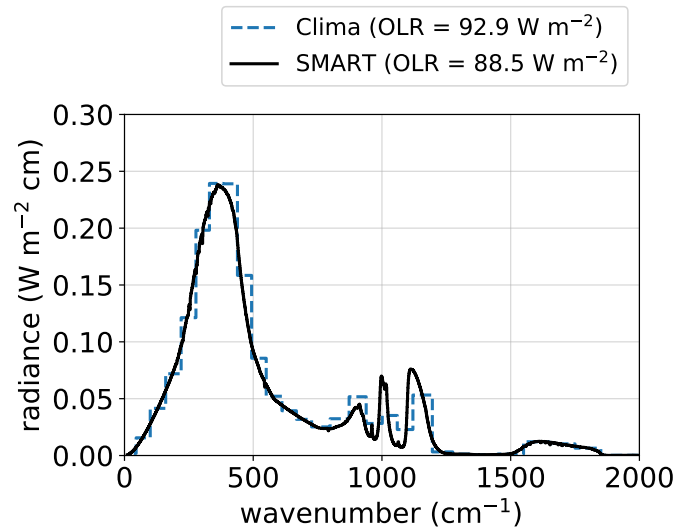
To simulate the climate of post-impact atmospheres, we developed a new radiative transfer and climate code called *Clima*. We approximately solve the radiative transfer equation using standard two-stream methods (Toon et al. 1989). The code includes opacities representing photolysis, Rayleigh scattering, collision-induced absorption, and approximates line absorption with k-distributions. All available opacities and citations, except photolysis cross sections, are listed in Table A2. In this article, to account for line absorption of multiple species, we use the “random overlap with resorting and rebinning” method described in Amundsen et al. (2017).

Figure A11 shows a thermal emission spectra computed with *Clima* for a two bar pure  $\text{CO}_2$  atmosphere on Mars with a 250 K surface temperature. This same benchmark has been computed by several other radiative transfer codes: SOCRATES (Wolf et al. 2022, Figure 2), ExoRT (Wolf et al. 2022, Figure 2), SMART (Figure A11), and the radiative transfer code used in Kopparapu et al. (2013) (their Figure 1). All codes estimate the total outgoing thermal energy to be between 86 and 94  $\text{W m}^{-2}$ , which is comparable to the value computed by *Clima* (92.9  $\text{W m}^{-2}$ ).

The *Clima* code also includes an adiabatic climate model. Given partial pressures of gases at the surface, the code draws a pseudoadiabatic temperature profile upward using Equation (1) in Graham et al. (2021) until the temperature



**Figure A10.** The deposition velocity of HCN caused by hydrolysis in the ocean. Calculations use Equation (C32) assuming  $v_{\text{over}} = 1.2 \times 10^{-5} \text{ cm s}^{-1}$ ,  $z_s = 10^4 \text{ cm}$ ,  $z_d = 4 \times 10^5 \text{ cm}$ .



**Figure A11.** Outgoing longwave radiation of a 2 bar  $\text{CO}_2$  atmosphere on Mars with a 250 K surface temperature, computed with *Clima* (this work) and SMART (Meadows & Crisp 1996). The agreement between the two codes validates *Clima*.

reaches an assume isothermal stratosphere. The code is general and can consider any number of condensing species, but  $\text{H}_2\text{O}$  is the only relevant condensible for post-impact atmospheres. Finally, to find an equilibrium climate, we solve a nonlinear equation for the surface temperature that balances incoming solar and outgoing longwave radiation. Each iteration of the nonlinear solve involves drawing an adiabat upward then computing the solar and infrared radiative fluxes.

The version of *Clima* used in this article (v0.3.1) is archived on Zenodo (<https://doi.org/10.5281/zenodo.7802952>), while the most up-to-date version can be found on GitHub (<https://github.com/Nicholaswogan/clima>).

## REFERENCES

- |   |   |
|---|---|
| <p>Adriani, A., Dinelli, B., Lopez-Puertas, M., et al. 2011, <i>Icarus</i>, 214, 584</p> <p>Amundsen, D. S., Tremblin, P., Manners, J., Baraffe, I., &amp; Mayne, N. J. 2017, <i>Astronomy &amp; Astrophysics</i>, 598, A97</p> <p>Arney, G., Domagal-Goldman, S. D., Meadows, V. S., et al. 2016, <i>Astrobiology</i>, 16, 873</p> | <p>Aulbach, S., &amp; Stagno, V. 2016, <i>Geology</i>, 44, 751</p> <p>Bada, J. L., &amp; Korenaga, J. 2018, <i>Life</i>, 8, 55</p> <p>Bada, J. L., &amp; Lazcano, A. 2002, <i>Science</i>, 296, 1982</p> <p>Becker, S., Feldmann, J., Wiedemann, S., et al. 2019, <i>Science</i>, 366, 76</p> |
|---|---|

**Table A2.** Opacities used in the *Clima* radiative transfer code

Opacity type	Opacity	Notes	Citation
k-distributions <sup>a</sup>	H <sub>2</sub> O	HITEMP2010 for 0 to 30,000 cm <sup>-1</sup> and HITRAN2016 for 30,000 to 42,000 cm <sup>-1</sup> . Voigt lineshape with 25 cm <sup>-1</sup> cutoff. Assumes Earth air broadening coefficients. Plinth or base is removed because this opacity is combined with MT-CKD H <sub>2</sub> O continuum.	<a href="#">Rothman et al. (2010)</a> ; <a href="#">Gordon et al. (2017)</a>
	CO <sub>2</sub>	HITEMP2010. Sub-Lorentzian lineshape with 500 cm <sup>-1</sup> cutoff. Assumes self-broadening coefficients.	<a href="#">Rothman et al. (2010)</a>
	CH <sub>4</sub>	HITEMP2020. Voigt lineshape with 25 cm <sup>-1</sup> cutoff. Assumes Earth air broadening coefficients.	<a href="#">Hargreaves et al. (2020)</a>
	CO	HITEMP2019. Voigt lineshape with 25 cm <sup>-1</sup> cutoff. Assumes self-broadening coefficients.	<a href="#">Li et al. (2015)</a>
	O <sub>2</sub>	HITRAN2016. Voigt lineshape with 25 cm <sup>-1</sup> cutoff. Assumes Earth air broadening coefficients.	<a href="#">Gordon et al. (2017)</a>
	O <sub>3</sub>	HITRAN2016. Voigt lineshape with 25 cm <sup>-1</sup> cutoff. Assumes Earth air broadening coefficients.	<a href="#">Gordon et al. (2017)</a>
CIA	H <sub>2</sub> -H <sub>2</sub>	-	<a href="#">Mollière et al. (2019)</a>
	H <sub>2</sub> -He	-	<a href="#">Mollière et al. (2019)</a>
	N <sub>2</sub> -N <sub>2</sub>	-	<a href="#">Mollière et al. (2019)</a>
	CH <sub>4</sub> -CH <sub>4</sub>	-	<a href="#">Karman et al. (2019)</a>
	N <sub>2</sub> -O <sub>2</sub>	-	<a href="#">Karman et al. (2019)</a>
	O <sub>2</sub> -O <sub>2</sub>	-	<a href="#">Karman et al. (2019)</a>
	H <sub>2</sub> -CH <sub>4</sub>	-	<a href="#">Karman et al. (2019)</a>
	CO <sub>2</sub> -CO <sub>2</sub>	-	<a href="#">Karman et al. (2019)</a>
	CO <sub>2</sub> -CH <sub>4</sub>	-	<a href="#">Karman et al. (2019)</a>
	CO <sub>2</sub> -N <sub>2</sub>	-	<a href="#">Karman et al. (2019)</a>
	N <sub>2</sub> -H <sub>2</sub>	-	<a href="#">Karman et al. (2019)</a>
Rayleigh scattering <sup>b</sup>	N <sub>2</sub>	-	<a href="#">Keady &amp; Kilcrease (2002)</a> ; <a href="#">Penndorf (1957)</a>
	CO <sub>2</sub>	-	<a href="#">Keady &amp; Kilcrease (2002)</a> ; <a href="#">Shemansky (1972)</a>
	O <sub>2</sub>	-	<a href="#">Keady &amp; Kilcrease (2002)</a> ; <a href="#">Penndorf (1957)</a>
	H <sub>2</sub> O	-	<a href="#">Keady &amp; Kilcrease (2002)</a> ; <a href="#">Ranjan &amp; Sassellov (2017)</a> ; <a href="#">Murphy (1977)</a>
	H <sub>2</sub>	-	<a href="#">Keady &amp; Kilcrease (2002)</a>

<sup>a</sup> All k-distributions are computed using HELIOS-K ([Grimm et al. 2021](#)).<sup>b</sup> Rayleigh scattering opacities are computed using a parameterization from [Vardavas & Carver \(1984\)](#).

- Behnel, S., Bradshaw, R., Citro, C., et al. 2010, *Computing in Science & Engineering*, 13, 31
- Benner, S. A., Bell, E. A., Biondi, E., et al. 2020, *ChemSystemsChem*, 2, e1900035
- Catling, D. C., & Kasting, J. F. 2017, *Atmospheric Evolution on Inhabited and Lifeless Worlds* (Cambridge University Press)
- Cech, T. R. 2012, *Cold Spring Harbor perspectives in biology*, 4, a006742
- Chameides, W., & Walker, J. C. 1981, *Origins of life*, 11, 291
- Citron, R. I., & Stewart, S. T. 2022, *The Planetary Science Journal*, 3, 116
- Claire, M. W., Sheets, J., Cohen, M., et al. 2012, *The Astrophysical Journal*, 757, 95
- Cui, J., Yelle, R., Vuitton, V., et al. 2009, *Icarus*, 200, 581
- Di Giulio, M. 1997, *Journal of molecular evolution*, 45, 571
- Ehhalt, D., Heidt, L., Lueb, R., & Pollock, W. 1975, *Pure and Applied Geophysics*, 113, 389
- Furukawa, Y., Nakazawa, H., Sekine, T., & Kakegawa, T. 2007, *Earth and Planetary Science Letters*, 258, 543
- Genda, H., Brasser, R., & Mojzsis, S. 2017, *Earth and Planetary Science Letters*, 480, 25
- Goldblatt, C., & Zahnle, K. J. 2011, *Climate of the Past*, 7, 203
- Goldman, A. D., & Kacar, B. 2021, *Journal of Molecular Evolution*, 89, 127
- Goodwin, D. G., Moffat, H. K., Schoegl, I., Speth, R. L., & Weber, B. W. 2022, doi: [10.5281/zenodo.6387882](https://doi.org/10.5281/zenodo.6387882)
- Gordon, I. E., Rothman, L. S., Hill, C., et al. 2017, *Journal of Quantitative Spectroscopy and Radiative Transfer*, 203, 3
- Graham, R., Lichtenberg, T., Boukrouche, R., & Pierrehumbert, R. T. 2021, *The Planetary Science Journal*, 2, 207
- Grimm, R. E., & Marchi, S. 2018, *Earth and Planetary Science Letters*, 485, 1, doi: [10.1016/j.epsl.2017.12.043](https://doi.org/10.1016/j.epsl.2017.12.043)
- Grimm, S. L., Malik, M., Kitzmann, D., et al. 2021, *The Astrophysical Journal Supplement Series*, 253, 30
- Hargreaves, R. J., Gordon, I. E., Rey, M., et al. 2020, *The Astrophysical Journal Supplement Series*, 247, 55
- Hindmarsh, A. C., Brown, P. N., Grant, K. E., et al. 2005, *ACM Transactions on Mathematical Software (TOMS)*, 31, 363
- Hirschmann, M. M., & Withers, A. C. 2008, *Earth and Planetary Science Letters*, 270, 147
- Holland, H. D. 1984, *The Chemical Evolution of the Atmosphere and Oceans* (Princeton University Press)
- Hörs, S. M. 2017, *Journal of Geophysical Research: Planets*, 122, 432
- Ircovitz, J. P., Rae, A. S., Citron, R. I., et al. 2022, *The Planetary Science Journal*, 3, 115
- Kadoya, S., Krissansen-Totton, J., & Catling, D. C. 2020, *Geochemistry, Geophysics, Geosystems*, 21, e2019GC008734
- Karman, T., Gordon, I. E., van Der Avoird, A., et al. 2019, *Icarus*, 328, 160
- Keady, J., & Kilcrease, D. 2002, in *Allen's Astrophysical Quantities* (Springer), 95–120
- Keefe, A. D., & Miller, S. L. 1996, *Origins of Life and Evolution of the Biosphere*, 26, 111
- Kharcha, P., Kasting, J., & Siefert, J. 2005, *Geobiology*, 3, 53
- Kopparapu, R. K., Ramirez, R., Kasting, J. F., et al. 2013, *The Astrophysical Journal*, 765, 131
- Korenaga, J. 2021, *Life*, 11, 1142
- Kress, M. E., & McKay, C. P. 2004, *Icarus*, 168, 475
- Kress, V. C., & Carmichael, I. S. 1991, *Contributions to Mineralogy and Petrology*, 108, 82
- Krissansen-Totton, J., Kipp, M. A., & Catling, D. C. 2021, *Geobiology*, 19, 342
- Lavvas, P., Coustenis, A., & Vardavas, I. 2008a, *Planetary and Space Science*, 56, 27
- . 2008b, *Planetary and Space Science*, 56, 67
- Leconte, J., Selsis, F., Hersant, F., & Guillot, T. 2017, *Astronomy & Astrophysics*, 598, A98
- Lewis, J. S. 1992, *Space resources materials: National Aeronautics and Space Administration Special Publication*, 509, 59
- Li, G., Gordon, I. E., Rothman, L. S., et al. 2015, *The Astrophysical Journal Supplement Series*, 216, 15
- Loison, J., Hébrard, E., Dobrijevic, M., et al. 2015, *Icarus*, 247, 218
- Marchi, S., Bottke, W., Elkins-Tanton, L., et al. 2014, *Nature*, 511, 578
- Marten, A., Hidayat, T., Biraud, Y., & Moreno, R. 2002, *Icarus*, 158, 532
- Massie, S., & Hunten, D. 1981, *Journal of Geophysical Research: Oceans*, 86, 9859
- Meadows, V. S., & Crisp, D. 1996, *Journal of Geophysical Research: Planets*, 101, 4595
- Miyakawa, S., James Cleaves, H., & Miller, S. L. 2002, *Origins of Life and Evolution of the Biosphere*, 32, 195
- Mollière, P., Wardenier, J., Van Boekel, R., et al. 2019, *Astronomy & Astrophysics*, 627, A67
- Muller, F., Escobar, L., Xu, F., et al. 2022, *Nature*, 605, 279
- Murphy, W. F. 1977, *The Journal of Chemical Physics*, 67, 5877
- Nicklas, R. W. 2019, PhD thesis, University of Maryland, College Park

- Okamura, H., Crisp, A., Hübner, S., et al. 2019, *Angewandte Chemie International Edition*, 58, 18691
- Patel, B. H., Percivalle, C., Ritson, D. J., Duffy, C. D., & Sutherland, J. D. 2015, *Nature Chemistry*, 7, 301
- Pearce, B. K., Molaverdikhani, K., Pudritz, R. E., Henning, T., & Cerrillo, K. E. 2022, *The Astrophysical Journal*, 932, 9
- Penndorf, R. 1957, *Journal of the Optical Society of America*, 47, 176
- Powner, M. W., Gerland, B., & Sutherland, J. D. 2009, *Nature*, 459, 239
- Ranjan, S., & Sasselov, D. D. 2017, *Astrobiology*, 17, 169
- Rimmer, P. B., & Rugheimer, S. 2019, *Icarus*, 329, 124
- Rimmer, P. B., & Shorttle, O. 2019, *Life*, 9, 12
- Ritson, D. J., Poplawski, M. W., Bond, A. D., & Sutherland, J. D. 2022, *Journal of the American Chemical Society*, 144, 19447
- Rothman, L. S., Gordon, I., Barber, R., et al. 2010, *Journal of Quantitative Spectroscopy and Radiative Transfer*, 111, 2139
- Sagan, C., & Chyba, C. 1997, *Science*, 276, 1217
- Sanchez, R. A., Ferbis, J. P., & Orgel, L. E. 1967, *Journal of Molecular Biology*, 30, 223
- Sasselov, D. D., Grotzinger, J. P., & Sutherland, J. D. 2020, *Science Advances*, 6, eaax3419
- Schmider, D., Maier, L., & Deutschmann, O. 2021, *Industrial & Engineering Chemistry Research*, 60, 5792
- Shemansky, D. 1972, *The Journal of Chemical Physics*, 56, 1582
- Sleep, N. H., Zahnle, K. J., Kasting, J. F., & Morowitz, H. J. 1989, *Nature*, 342, 139
- Stribling, R., & Miller, S. L. 1987, *Origins of Life and Evolution of the Biosphere*, 17, 261
- Strobel, D. F., Atreya, S. K., Bézard, B., et al. 2009, *Titan from Cassini-Huygens*, 235
- Sutherland, J. D. 2016, *Angewandte Chemie International Edition*, 55, 104
- Takahashi, E. 1986, *Journal of Geophysical Research: Solid Earth*, 91, 9367
- Thompson, M. A., Krissansen-Totton, J., Wogan, N., Telus, M., & Fortney, J. J. 2022, *Proceedings of the National Academy of Sciences*, 119, e2117933119
- Tian, F., Kasting, J., & Zahnle, K. 2011, *Earth and Planetary Science Letters*, 308, 417
- Todd, Z. R., Lozano, G. G., Kufner, C. L., Sasselov, D. D., & Catling, D. C. 2022, *Geochimica et Cosmochimica Acta*, 335, 1
- Todd, Z. R., & Öberg, K. I. 2020, *Astrobiology*, 20, 1109
- Toner, J. D., & Catling, D. C. 2019, *Geochimica et Cosmochimica Acta*, 260, 124
- Toon, O. B., McKay, C., Ackerman, T., & Santhanam, K. 1989, *Journal of Geophysical Research: Atmospheres*, 94, 16287
- Trainer, M. G., Pavlov, A. A., DeWitt, H. L., et al. 2006, *Proceedings of the National Academy of Sciences*, 103, 18035
- Urey, H. C. 1952, *Proceedings of the National Academy of Sciences*, 38, 351
- Vardavas, I., & Carver, J. H. 1984, *Planetary and Space Science*, 32, 1307
- Vuitton, V., Yelle, R., & Anicich, V. 2006, *The Astrophysical Journal*, 647, L175
- White, H. B. 1976, *Journal of molecular evolution*, 7, 101
- Wogan, N., Catling, D., Zahnle, K., & Claire, M. 2022, *Proceedings of the National Academy of Sciences*
- Wogan, N., Krissansen-Totton, J., & Catling, D. C. 2020, *The Planetary Science Journal*, 1, 58
- Wolf, E., & Toon, O. 2010, *Science*, 328, 1266
- Wolf, E. T., Kopparapu, R., Haqq-Misra, J., & Fauchez, T. J. 2022, *The Planetary Science Journal*, 3, 7
- Yadav, M., Kumar, R., & Krishnamurthy, R. 2020, *Chemical reviews*, 120, 4766
- Zahnle, K., Marley, M. S., Morley, C. V., & Moses, J. I. 2016, *The Astrophysical Journal*, 824, 137
- Zahnle, K. J. 1986, *Journal of Geophysical Research: Atmospheres*, 91, 2819
- Zahnle, K. J., Lupu, R., Catling, D. C., & Wogan, N. 2020, *The Planetary Science Journal*, 1, 11
- Zahnle, K. J., & Marley, M. S. 2014, *The Astrophysical Journal*, 797, 41